

THESIS FOR THE DEGREE OF DOCTOR OF PHILOSOPHY IN SOLID AND
STRUCTURAL MECHANICS

On Cohesive Modelling of Carbon/Epoxy Composites

Delamination and Fibre Compressive Failure

DANIEL SVENSSON

Department of Applied Mechanics
CHALMERS UNIVERSITY OF TECHNOLOGY

Göteborg, Sweden 2015

On Cohesive Modelling of Carbon/Epoxy Composites
Delamination and Fibre Compressive Failure
DANIEL SVENSSON
ISBN 978-91-7597-214-5

© DANIEL SVENSSON, 2015

Doktorsavhandlingar vid Chalmers tekniska högskola
Ny serie nr. 3895
ISSN 0346-718X
Department of Applied Mechanics
Chalmers University of Technology
SE-412 96 Göteborg
Sweden
Telephone: +46 (0)31-772 1000

Chalmers Reproservice
Göteborg, Sweden 2015

On Cohesive Modelling of Carbon/Epoxy Composites
Delamination and Fibre Compressive Failure
Thesis for the degree of Doctor of Philosophy in Solid and Structural Mechanics
DANIEL SVENSSON
Department of Applied Mechanics
Chalmers University of Technology

ABSTRACT

Carbon Fibre Reinforced Polymers (CFRP) are widely used in engineering applications where weight saving and high mechanical performance are key factors. However, an inherent weakness of laminated CFRP:s is their relatively low resistance to delamination. The first part of this thesis is devoted to methods to extract cohesive laws associated with delamination. The method is based on fracture mechanical tests and measurement of the displacement field close to the crack tip. Pure mode cohesive laws are determined by an optimization procedure involving finite element (FE) simulations. An initiation based formulation allows for a straight forward determination of the mixed mode cohesive law. FE simulations show that the fracture loads and local displacements are in good agreement with the experiments.

The second part of the thesis is concerned with mixed mode cohesive modelling under small scale yielding conditions. Under such loading conditions, a robust cohesive model should conform to the predictions of linear elastic fracture mechanics. Both isotropic and orthotropic adjacent continuums under plane stress or plane strain are treated. By analytical derivations, it is concluded that two conditions are sufficient for mixed mode cohesive laws to achieve this property. These design rules address the choice of initial cohesive stiffnesses and the formulation of the softening response during mixed mode cohesive separations. Validating FE-simulations where SSY conditions are imposed on a circular domain support the results. It is also demonstrated that this minimizes the discrepancy to LEFM predictions for fracture mechanical specimens where boundary effects influence the elastic fields close to the crack tip.

The third part of the thesis focuses on a failure type entirely different from delamination: longitudinal compressive failure. In a CFRP, almost all the load is carried by the fibres. With compressive strengths along the fibre direction substantially lower than the tensile strength, prediction of longitudinal compressive failure plays a key role in the design of structural CFRP components. The dominating failure mode due to longitudinal compression is kink-band formation. The objective in the third part is to extract the cohesive law associated with kink-band formation. Equilibrium of configurational forces is used for this purpose. Identified configurational forces are continuously measured by monitoring the displacements field on the specimen's lateral surface. The kink-band is formed in the intended region of the specimen and the evaluation shows a peak stress and fracture energy in the anticipated ranges.

Keywords: CFRP, Cohesive zone model, J-integral, LEFM, Delamination, Compressive failure

to Anna and Liam

PREFACE

The work presented in this thesis has been carried out at the School of Engineering Science at University of Skövde in co-operation with the Department of Applied Mechanics at Chalmers University of Technology between the years 2010-2015. Funding from the Swedish National Aeronautical Research Program and the Swedish Knowledge Foundation is gratefully acknowledged.

First of all I would like to express my sincerest gratitude to my co-supervisor Associate Professor Svante Alfredsson. With an impressive patience, he has always been there to support and guide me during all stages of my PhD studies. I am also grateful to my main supervisor Professor Ulf Stigh for generously sharing his time and knowledge during this time.

I would also like to thank my present and former colleagues in the Mechanics of Materials group for their helpful and friendly attitude during these years and other colleagues at the School of Engineering and Science at the University of Skövde for creating such an enjoyable working atmosphere.

Finally, and most importantly, my deepest gratitude goes to my family. Most of all I want to thank Anna for all her love and support during these years and our little boy Liam for always putting a smile on my face. You are the sunshine of our lives.

Daniel Svensson
Skövde, May 2015

THESIS

This thesis consists of an extended summary and the following appended papers:

- Paper A** D. Svensson, K.S. Alfredsson, A. Biel and U. Stigh. Measurement of cohesive laws for interlaminar failure of CFRP. *Composite Science and Technology* **100** (2014), 53-62
- Paper B** D. Svensson, K.S. Alfredsson and U. Stigh. Measurement of mixed mode cohesive laws for interlaminar failure of CFRP. *Submitted for international publication*
- Paper C** D. Svensson, K.S. Alfredsson and U. Stigh. On cohesive modelling of mixed mode crack nucleation in anisotropic solids - the interplay between bulk and cohesive stiffnesses. *Submitted for international publication*
- Paper D** D. Svensson, K.S. Alfredsson, U. Stigh and N.E. Jansson. Measurement of cohesive law for kink-band formation in unidirectional composite. *Submitted for international publication*

The appended papers have been prepared in collaboration with the co-workers. The contributions of the author of this thesis are listed below.

Paper A

Planned the paper with Alfredsson and Stigh. Performed the experiments with Biel. Evaluated the experiments. Performed the simulations. Wrote the paper in collaboration with Alfredsson. Stigh proof-read the paper and added valuable suggestions throughout the work.

Paper B

Planned the paper with the co-authors. Performed the experiments in collaboration with Biel. Evaluated the experiments. Conducted the theoretical development and wrote the paper in collaboration with Alfredsson. Performed the simulations. Stigh proof-read the paper and added valuable suggestions throughout the work.

Paper C

Planned the paper with the co-authors. Conducted the theoretical development and wrote the paper in collaboration with Alfredsson. Performed the simulations. Stigh proof-read the paper and added valuable suggestions throughout the work.

Paper D

Planned the paper with Stigh and Alfredsson. Took part in designing the experiments together with Stigh and Jansson. Conducted the theoretical development in collaboration

Stigh and Alfredsson. Performed the experiments together with Biel. Evaluated the experiments. Wrote the paper together with Stigh and Alfredsson.

CONTENTS

Abstract	i
Preface	v
Thesis	vii
Contents	ix
I Extended Summary	1
1 Introduction	2
1.1 Background and motivation	2
1.2 Types of CFRP materials in this thesis	6
1.3 Failure modes in CFRP	8
1.4 Objectives and scope	9
2 Fracture mechanics	9
2.1 Linear elastic fracture mechanics	9
2.2 The J -integral	13
3 The cohesive zone model	16
3.1 Types of cohesive laws	20
3.2 Cohesive zones and the J -integral	21
3.3 Influence of cohesive parameters	23
3.4 Element size requirements	26
3.5 Initial stiffnesses	26
3.6 Cohesive zones and LEFM	27
3.7 Discussion of the results in paper C	27
4 Delamination	28
4.1 Sources of delamination	28
4.2 In-situ observations of delamination growth	30
4.3 Characterisation of delamination resistance	33
4.4 Interlaminar strengths	35
4.5 Objective and method in paper A and B	36
5 Longitudinal compressive failure	37
5.1 Kink-band formation	37
5.2 Measurement of the fracture energy	38
5.3 Objective and method in paper D	39

6	Summary of appended papers	40
7	Future work	41
	References	42
II	Appended Papers A-D	51

Part I
Extended Summary

1 Introduction

1.1 Background and motivation

Improved mechanical performance and weight reduction are the driving forces for the increasing usage of advanced composite materials in structural applications. Carbon Fibre Reinforced Polymers (CFRP) combine strong and stiff carbon fibres with a load transferring and protective polymer matrix material. The CFRP:s considered in this thesis are continuous fibre composites sometimes called long fibre composites. A laminated CFRP is schematically sketched in Fig. 1.1. Plies, also referred to as laminae, are thin layers consisting of the two basic constituents, i.e. aligned carbon fibres and the polymer matrix. The laminate is built up by stacking plies of varying fibre orientations.

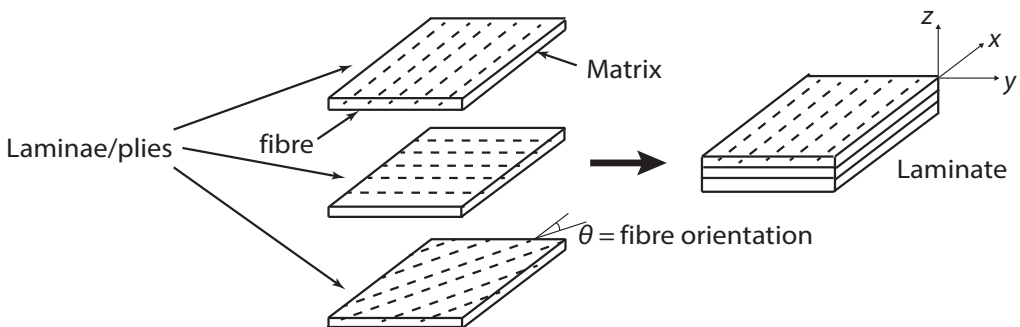


Figure 1.1: Schematic sketch of a laminated CFRP. Picture re-drawn from [1].

The main advantage of CFRP is their excellent specific stiffness and strength in the x - y -plane. When tailoring fibre orientations efficiently, considerably higher specific stiffness and strength are achieved than for traditional engineering materials, e.g. steel and aluminium. Mainly due to the weight saving potential, CFRP:s are heavily utilized in many engineering fields and products, e.g. aeronautical, aerospace, naval, wind energy, automotive, sport equipment and a wide range of civil constructions, e.g. pipes and reinforcement of bridges. The aeronautical industry can be considered to be leading the aggressive development towards an extended use of CFRP and other advanced composite materials. At the early stages, this development was mainly driven by the military industry but has lately been overtaken by the civil aircraft industry to counter the rising fuel prices, environmental impact and the desire to enhance the range/payload ratio. Besides the high specific mechanical properties, the superior resistance to corrosion and fatigue are very beneficial. This enables longer inspection intervals that decreases the maintenance cost [2]. The usage of advanced composite materials in commercial aircrafts has increased rapidly the last decade. An example of this is the Boeing 787 Dreamliner aircraft, that comprises CFRP and other composite materials to about 50 % of the material weight, cf. Fig. 1.2.

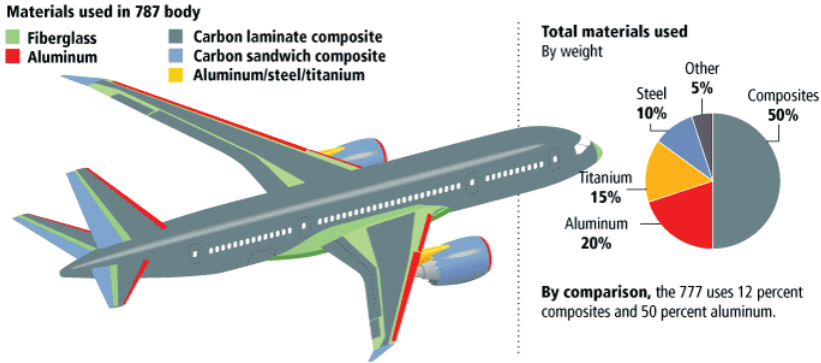


Figure 1.2: The Boeing 787 Dreamliner. Picture from Boeing [3].

CFRP laminates are used on primary parts, i.e. the fuselage, wings, tail and doors, which allows for a considerable weight reduction as compared to previous designs where aluminium was used to a larger extent. To create an efficient design of the airframe, the obvious aim is to use the optimum material for the specific application of the component. CFRP:s are preferred for components that are highly tension-loaded while other materials, e.g. aluminium, are still used at regions subjected to substantial compressive loads [2]. Typically, the substitution from aluminium to composites offers on average a weight reduction of 20-30 % for the component [4].

Due to the strong heterogeneity and anisotropy, CFRP:s exhibit complex failure mechanisms that are challenging to predict. A wide range of failure modes may initiate and interact to subsequently control ultimate failure of the component. Moreover, the material behaviour may depend on a number of factors, e.g. moisture, temperature, stacking sequences, size effects, load combinations and sequences. Therefore, the design and certification of structural (load carrying) parts require a comprehensive and costly testing campaign that range from coupon tests to full scale testing. These tests must demonstrate sufficient static strength, residual strength after fatigue loading and damage-tolerance, i.e. the damaged materials ability to retain sufficient load carrying capacity. The certification process in the aeronautical industry utilizes the building-block approach [5], where analyses are verified by physical testing at all levels of the product development. This is usually represented by the test pyramid shown in Fig. 1.3.

Firstly, thousands of coupon tests are conducted to generate a statistical database of the basic material properties and to quantify the scatter [6]. Design allowables are determined from these results, e.g. in terms of conservative strain measures. Tests are then performed with increasing level of complexity to investigate the influence of new features introduced at each level. For example, bolted joints or bonded attachments that are introduced at the element level. Further along the certification process, structural tests are performed on assembled sub-components and finally, tests are carried out on full scale components and even the entire aircraft. The loading conditions applied to the full scale component aims to reproduce those experienced during service of the component.

For example, in the certification of the complete wing of a Boeing 787, the wing was bended upwards beyond the ultimate load to demonstrate its safe design [6].

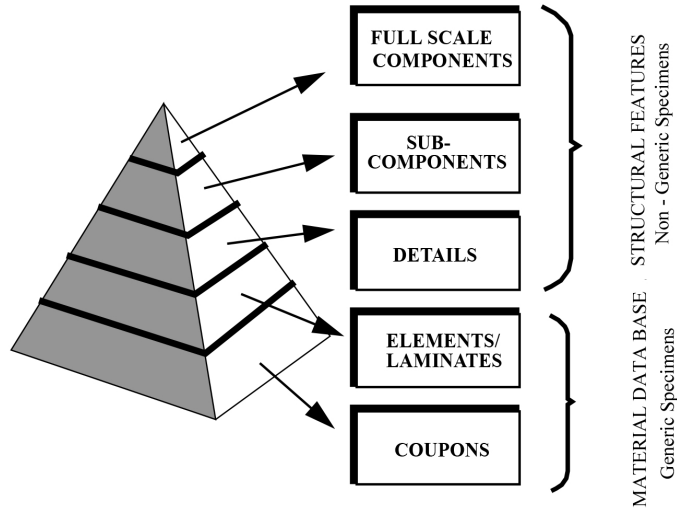


Figure 1.3: Test pyramid illustrating the different complexity levels in the certification program. Picture: courtesy of professor Tonny Nyman, SAAB Aeronautics/Royal Institute of Technology, Sweden.

To account for the presence of damage, damage-tolerance of the composite structure needs to be demonstrated for more built up structures. Defects may be present from the manufacturing process or arise during harsh working conditions such as impact loads. Within the damage-tolerance concept, it is required that defects have no-growth characteristics or do not grow to critical size depending on the severity of the defect. Defects on the threshold of detectability, i.e. barely visible damage, must display no-growth characteristics, i.e. they will not grow under normal working conditions. In the design phase, the presence of such defects is often accounted for in the model or test by including an equivalent artificial defect of comparable size [7].

Due to the large cost and time consumption associated with the testing campaign, it is desirable to increase the analysis capability in order to replace parts of the physical tests with virtual tests. The associated cost of an individual test increases rapidly as the complexity level increases. However, it is anticipated that full-scale testing will be required for the certification of aircrafts also in the future. The primary goal is therefore to replace tests at the intermediate complexity levels by virtual testing [8]. Thus, within the research community, there is a driving force to formulate analytical and numerical models that enable accurate prediction of damage growth and subsequent failure of composites.

Stress based models may often be used to predict initiation of damage and, under some circumstances, even to predict failure. However, critical regions are often located at material and geometrical discontinuities where singular stresses are predicted which

make stress based criteria inappropriate. Moreover, assuming an ideally brittle material is normally not sufficient to predict the failure load of the laminate even though CFRP generally exhibits an apparent brittle behaviour. Various damage mechanisms may dissipate energy prior to macroscopic failure. This may delay the final collapse. For example in the open hole tension test shown in Fig. 1.4, damage in the form of matrix cracking and delamination initiate at the hole boundary well before the critical load is reached [9]. This leads to a redistribution of stresses and further load may be applied prior to failure. Thus, stress based dimensioning to avoid damage initiation often leads to overly conservative design, i.e. it generates excessive safety factors. Moreover, the strength of composite laminates subjected to tensile and compressive loading has been shown to be size dependent, e.g. [10, 11, 12]. Thus, for an accurate prediction, the model should incorporate a length scale and reflect the inelastic processes that precede failure.

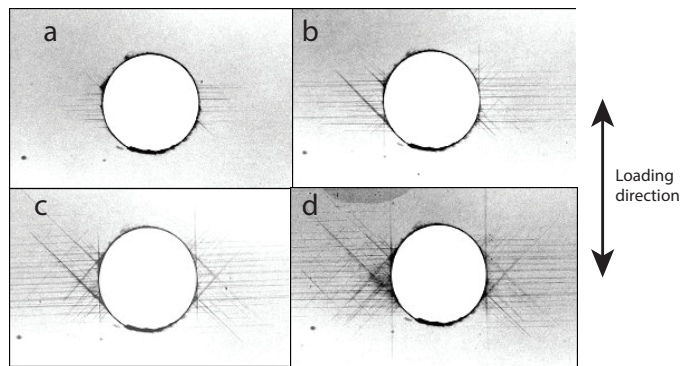


Figure 1.4: X-ray image of the damage development during an open hole tension test at: a) 36 % b) 57 % b) 78 % d) 93 % of the failure load. Figure from [9].

One method to resolve these issues are offered by the Cohesive Zone Model (CZM). Initiation of inelasticity is modelled with a stress criterion and the subsequent propagation is diagnosed by an energy criterion inherent to the fracture mechanics approach discussed in chapter 2. The continuous loss of integrity towards failure can be modelled using a wide variety of cohesive laws that suits the phenomena that is aimed to be modelled. A discussion on the CZM and various cohesive law formulations are given in chapter 3.

In this thesis, the CZM concept is utilized to model the failure modes in CFRP denoted delamination and longitudinal compressive failure. More detailed discussions of these failure modes are given in chapter 4 and 5, respectively.

1.2 Types of CFRP materials in this thesis

Two different types of CFRP:s are used for the studies in this thesis. In papers A-B, experiments are conducted on a pre-impregnated tape material often abbreviated as prepreg materials. In paper D, a material is studied that is characterised as a Non-Crimp Fabric (NCF) composite. A detailed discussion on NCF:s is given in [13]. Common for both materials is the clear laminated structure with distinct plies of aligned carbon fibres as schematically illustrated in Fig. 1.1.

Prepregs are manufactured from thin layers of aligned carbon fibres that are pre-impregnated by epoxy resin. The laminate is formed by stacking the layers, usually about 0.125 mm thick, into a mould. The mould is then placed in an autoclave where the laminate is cured by increasing the pressure and temperature. A micrograph of a cross-ply prepreg laminate with a ply thickness of 0.25 mm is shown in Fig. 1.5. These materials are widely used in the aeronautical industry and offer a high fibre volume fraction and excellent in-plane stiffness and strength. However, due to the lack of reinforcement in through-the-thickness direction of the laminate, they are sensitive to out-of-plane stresses. In paper A-B, this property is characterised on the prepreg carbon/epoxy composite HTA/6376.

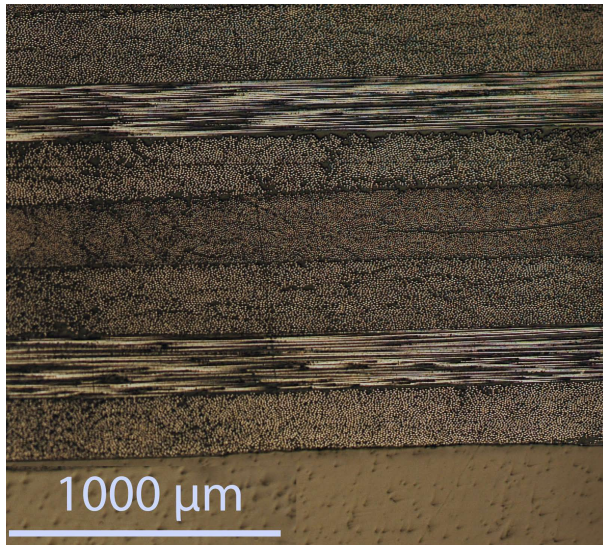


Figure 1.5: Micrograph of a prepreg laminate. Picture: courtesy of Dr. Fredrik Edgren (GKN Aerospace Sweden AB).

In the manufacturing of the NCF composite used in paper D, a dry preform of the reinforcement fabric is placed in a mould and impregnated by a liquid thermoset resin using resin transfer moulding. The preform is created by stacking several layers of unidirectional carbon fibre weave on top of each other. The unidirectional weave consists

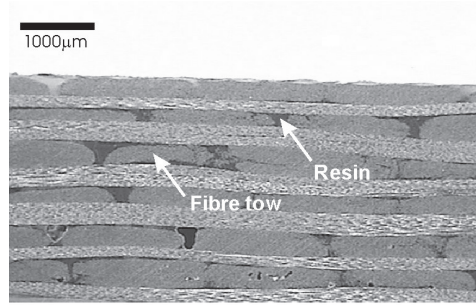


Figure 1.6: Micrograph NCF composite cross section. Picture from [14].

of carbon fibre bundles in the warp direction, held together by a woven scaffold structure of thin glass yarns. The focus of paper D is to characterise the behaviour associated with longitudinal compression, i.e. compressive loading in the fibre direction. In [13], two characteristics of NCF composites are discussed that influence the macroscopic compressive stiffness and strength. Both are observed at the meso-scale, i.e. at the lamina level. Firstly, distinct fibre bundles are visible that are separated from each other by resin rich areas, cf. Fig. 1.6. This allows carbon fibre bundles in neighbouring layers to nest together, causing waviness to the fibre bundles. In prepregs, a more homogeneous distribution of fibres within plies are observed, cf. Fig. 1.5. Waviness in the layers is also created by the woven textile structure of the fabric. The carbon fibre bundles are woven together with the thin weft yarns, causing waviness in the carbon bundles. The waviness of fibres reduces the compressive strength as well as the stiffness.

1.3 Failure modes in CFRP

In the fracture process of CFRP laminates, several failures modes usually occur and interact in a complex manner. The extent of each failure mode may vary from ply to ply depending on, e.g. the loading conditions and stacking sequence. The major failure modes are divided into three groups to facilitate the discussion in the following sections. The three groups denoted interlaminar, intralaminar and translaminar failures are depicted in Fig. 1.7 [15].

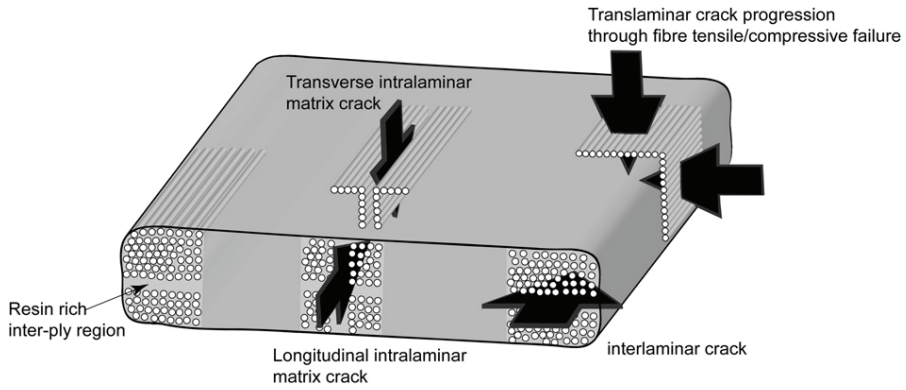


Figure 1.7: Illustration of the major failure modes in CFRP. Picture from [15].

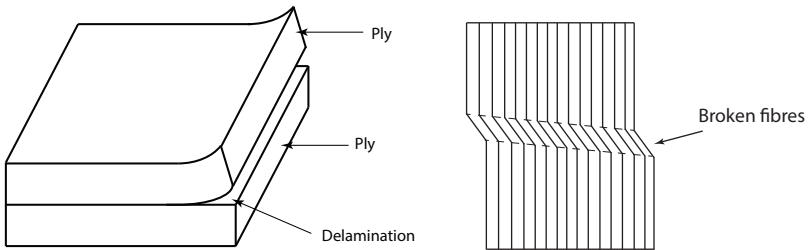


Figure 1.8: *Left*: Schematic sketch of delaminated plies. *Right*: Schematic sketch of a kink-band.

Interlaminar failure also referred to as delamination corresponds to fracture through separation of adjacent plies as depicted in Fig. 1.8a. Delamination is discussed in detail in chapter 4. Intralaminar failure corresponds to matrix cracking and matrix/fibre debonding within plies. Longitudinal intralaminar cracking is also referred to as splitting. Translaminar failures are fibre dominated failures and refer to tensile or compressive

failure perpendicular to the fibres. Failure due to longitudinal compression usually occurs by a local buckling process of the fibres leading to the formation of a kink-band. This corresponds to a band of broken fibres as shown in Fig. 1.8b. Longitudinal compressive failure is discussed in chapter 5.

1.4 Objectives and scope

The development of structural CFRP components requires a comprehensive test program including tests of various scales and levels of complexity cf. Fig. 1.3. With increased predictive capability, parts of the physical testing may gradually be reduced and excessive safety factors can be lowered. Ultimately, this could lead to better optimized structures while reducing the cost and thereby also promote an increased use of CFRP in more cost sensitive industries. An important step in the formulation of reliable predictive models is the ability to characterise individual failure modes in isolation.

The objective of this thesis is to, based on experimental measurements, extract cohesive laws for delamination and longitudinal compressive failure. Moreover, shortcomings of the CZM under mixed mode loading conditions are addressed in a combined analytical and numerical study.

2 Fracture mechanics

Fracture mechanics principles are commonly employed for the prediction of fracture in CFRP. The most wide spread use of fracture mechanics is found in the characterisation of the resistance against matrix and interface dominated failures such as delamination. However, fracture mechanical testing is also relatively common for translaminar failures such as longitudinal compressive failure. Examples of this are given for these types of failures in chapter 4 and 5, respectively. Furthermore, the CZM originates from the framework of fracture mechanics. Both concepts are extensively used in this thesis for the modelling the two failure modes considered. Thus, in this chapter, a brief background and some of the basic relations of fracture mechanics are presented to facilitate the discussion in the following chapters.

2.1 Linear elastic fracture mechanics

More than a hundred years ago, Inglis [16] showed the elastic stress field is amplified in regions near notches and that stresses increase as the radius of the notch decreases. About a decade later, Griffith was focusing on the prediction of fracture in brittle glass [17]. Experimental measurement showed that the strength was surprisingly low and also specimen size dependent. This could not be predicted by a simple stress analysis. Griffith suggested that the measured strengths could be explained by the presence of flaws in the material. However, the stress concentrations derived by Inglis could not predict on the flaw size dependency. An energy based fracture criterion was therefore proposed where crack growth occurs when the release of potential energy equals or exceeds the surface

energy required to create new crack surfaces. This release of potential energy per unit area is known as the energy release rate, G , sometimes referred to as the crack driving force. That is, with Π and a denoting the potential energy per unit width and the crack length, respectively, G is defined by

$$G = -\frac{d\Pi}{da}. \quad (2.1)$$

With this approach, Griffith was able to accurately predict the strength versus flaw size. However, the method was not applicable for metals and thereby not useful in many fields of engineering. Irwin extended Griffith's work of the energy release rate concept such that crack growth in metals could be predicted [18]. He noticed that the increased surface energy during fracture of metals is in principal negligible compared to the energy dissipated by the plastic deformation near the crack tip. Moreover, Irwin also found that G was related to the singular stress field in the vicinity of the crack tip. The amplitude of the singular stress was shown to scale with one parameter that is directly related to G , i.e. the stress intensity factor, K .

In the Linear Elastic Fracture Mechanics (LEFM) approach, crack growth is predicted when G or K reaches its critical value and the two formulations are completely equivalent. The critical values denoted the fracture energy G_c and the fracture toughness K_c , respectively, specify the material's resistance to fracture and are considered to be properties of the material.

The stress intensity factor and its components are given by solving a linear elastic boundary-value problem and depend on the loading and geometry of the specimen. A collection of stress intensity factors for various geometries and isotropic material are given in [19]. In [20], Sou et al. develops a rescaling technique where approximate stress intensity factors and stress concentration factors for orthotropic materials may be constructed from the isotropic case. This is exemplified by Bao et al. [21] for several test geometries.

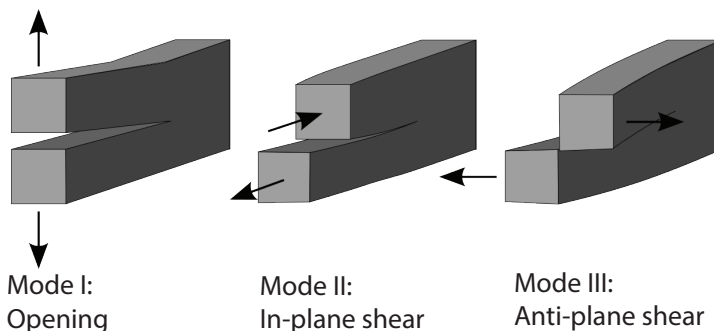


Figure 2.1: Illustration of the deformation modes. Picture from [22].

In LEFM, the loading of a crack front is divided into the three deformation modes shown in Fig. 2.1, i.e. the symmetric (mode I), the anti-symmetric (mode II) and the anti-plane

(mode III) part of loading. In this thesis, the discussion is restricted mode I and mode II. When LEFM applies the body can be analysed assuming linear elasticity. Thus, the modes of loading of the crack tip can be treated independently by superposition. That is, K and G may be divided into components associated with respective mode of loading, i.e.

$$G = G_I + G_{II} \quad K = K_I + K_{II}. \quad (2.2)$$

For isotropic materials, K and G are related by $G_I = K_I^2/\bar{E}$ and $G_{II} = K_{II}^2/\bar{E}$ where $\bar{E} = E$ for plane stress and $\bar{E} = E/(1 - \nu^2)$ for plane strain. Similar relations for anisotropic materials were derived by Sih et al. in [23]. This is discussed later in this section.

When a cracked body is subjected to remote loading, the stress field predicted by linear elasticity is given by the stress intensity factors. When no influence of the remote loading or end effects are present, the stresses at the crack tip are infinite and vary as $\sim r^{-1/2}$ where r denotes the distance from the crack tip. For a crack in the x - z -plane with the crack tip at $x = 0$, cf. Fig. 2.2a, the stress intensity factors are defined by [20]

$$\Sigma_y = \frac{K_I}{\sqrt{2\pi x}}, \quad T_{xy} = \frac{K_{II}}{\sqrt{2\pi x}}, \quad (2.3)$$

where Σ_y and T_{xy} denote the normal and shear stress along $y = 0$, respectively.

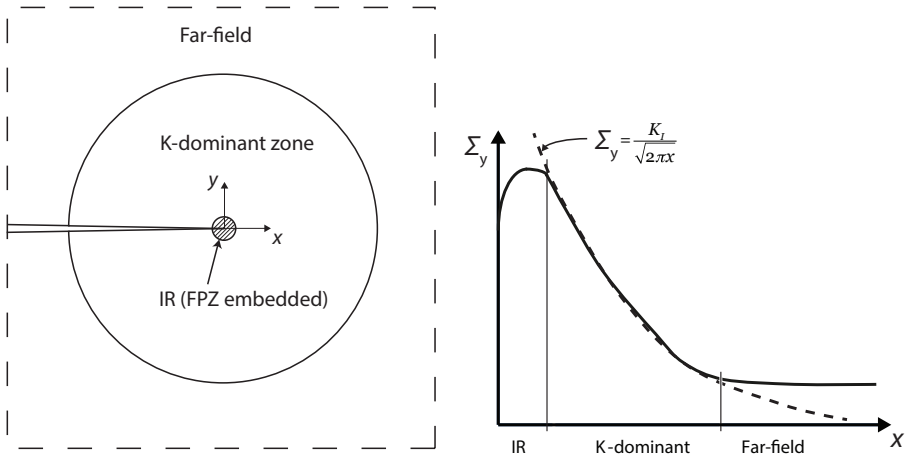


Figure 2.2: Illustration of SSY and the K -dominant zone. Right picture re-drawn from [24]

However, all materials have a limited strength. Thus, a Fracture Process Zone (FPZ) develops at the proximity of the crack tip where inelastic processes such as plastic deformation and microcracking take place. Outside of the FPZ, the body deforms linear elastically. LEFM requires Small-Scale-Yielding (SSY) or Small-Scale-Bridging (SSB) conditions referring to that the FPZ is very small compared to other characteristic dimensions of the body. Under such conditions, a region denoted the K -dominant region

exists. In this region, stresses and displacements are governed by the linear elastic solution, i.e. by the components of K . That is, within this zone, stresses and displacements obey the singular elastic field and are not influenced by the FPZ or boundary effects. This is illustrated in Fig. 2.2a, where three regions are indicated, i.e. the Influenced Region (IR), the K -dominant region and the far-field. The IR region contains the FPZ and adjacent elastically deforming points that are influenced by the FPZ. That is, the FPZ is embedded in the IR as shown in Fig. 2.2a. As shown, the extension of the K -dominant zone is limited by the far-field where the stresses and displacements are influenced by outer boundaries and remote loading. In Fig. 2.2b, the normal stress distribution ahead of the crack tip under SSY conditions is schematically sketched with a solid line and the singular stress field is indicated by dashed line.

The elastic stress, strain and displacement fields for an orthotropic material are formulated by Sih et al. in [23]. In [20], Sou et al. introduce two dimensionless parameters that fully characterise the orthotropy and thereby reduce the number of material parameters,

$$\lambda = \frac{s_{11}}{s_{22}}, \quad \rho = \frac{2s_{12} + s_{66}}{2\sqrt{s_{11}s_{22}}}, \quad (2.4)$$

where s_{ij} are the plane stress or the plane strain orthotropic compliances given in [25]. More specifically, with the generalized Hooke's law¹

$$\epsilon_i = \sum_j s_{ij}\sigma_j. \quad (2.5)$$

For plane stress conditions, the relevant components of s_{ij} for λ and ρ are,

$$s_{11} = \frac{1}{E_1}, \quad s_{22} = \frac{1}{E_2}, \quad s_{66} = \frac{1}{G_{12}}, \quad s_{12} = -\frac{\nu_{12}}{E_1} = -\frac{\nu_{21}}{E_2}, \quad (2.6)$$

where subscript 1 and 2 denote components in the x - and y -direction that coincide with the principal axes of the orthotropic material. Here, E_i is the Young's modulus in the i -direction, G_{12} is the shear modulus and ν_{ij} are the Poisson's ratios. For plane strain conditions, s'_{ij} replace s_{ij} in Eqs. (2.4)-(2.5) [20]

$$s'_{ij} = s_{ij} - s_{i3}s_{j3}/s_{33}. \quad (2.7)$$

Sou et al. showed that K and G for orthotropic materials can be approximated from isotropic solutions. For a crack along the x -direction, the λ -dependence can be derived explicitly by rescaling the x -axis by $\xi = \lambda^{1/4}x$. Thus, the calibration of G and K for different geometries depend on one material parameter only, i.e. ρ . In [21], Bao et al. calibrated this dependence with polynomials for several test specimens by numerical investigations using finite element analyses.

For plane stress, the relations between the energy release rates and stress intensity factors are in [23] given by

$$G_I = \left(s_{11}s_{22} \frac{1+\rho}{2} \right)^{1/2} \lambda^{-1/4} K_I^2, \quad G_{II} = \left(s_{11}s_{22} \frac{1+\rho}{2} \right)^{1/2} \lambda^{1/4} K_{II}^2. \quad (2.8)$$

¹Voight notation is adopted, i.e. $\epsilon_1 = \epsilon_x, \epsilon_2 = \epsilon_y, \dots, \epsilon_6 = \gamma_{xy}$ and $\sigma_1 = \sigma_x, \sigma_2 = \sigma_y, \dots, \sigma_6 = \tau_{xy}$.

For plane strain conditions, s'_{ij} replace s_{ij} in Eqs. (2.4) and (2.8).

In the formulation of G for a specific test specimen, one may derive the expression for K as discussed above and obtain G with Eq. (2.8). Fracture mechanical testing with the assumption of LEFM is often carried out on beam-like geometries, especially in characterisation of delamination resistance of CFRP. In such situations, the ERR is usually derived by the compliance method assuming beam theory. With this approach one may utilize the general expression, cf. e.g. [26]

$$G = -\frac{d\Pi}{da} = \frac{P^2}{b} \frac{dC}{da}, \quad (2.9)$$

where P , b , a and C are the applied load, specimen width, crack length and compliance respectively. With C expressed in terms of a , G may be formulated as a function of the applied load, the displacement of the loading point or a combination of thereof. If simple beam theory is used, correction factors are needed to account for orthotropy or the presence of a non-negligible shear force that complicate the deformation close to the crack tip. Such correction factors are given in [21] and in [27] several proposed formulations are examined for delamination testing of CFRP.

A third option for the derivation of the ERR is to utilize the J -integral [28]. This is a very useful tool since the assumption of SSY conditions is not required.

2.2 The J -integral

In the late 1960's, Rice introduced a line integral denoted the J -integral for the characterisation of the local deformation field near cracks, notches and other stress raising features in two-dimensional problems [28]. A severe difficulty to determine such deformation fields was identified, especially when the material around the notch-tip undergoes substantial non-linear deformation. By using the fact that the J -integral under favourable circumstances is integration path independent, Rice bypassed this difficulty. That is, the local deformation field near the notch-tip can be determined by studying the stress, strain and displacement field far away from the notch-tip that is sometimes straight forward to derive.

With, T_i , u_i , n_i and W denoting the traction vector, the displacement vector, the outward unit normal vector along an integration contour \mathcal{C} , cf. Fig. 2.3, and the strain energy density, respectively, the J -integral is given by,

$$J = \int_{\mathcal{C}} \left(W n_1 - T_i \frac{\partial u_i}{\partial x} \right) d\mathcal{C}, \quad (2.10)$$

where index notation is employed, repeated indexes indicates summation and $i=1,2$ indicates component in the x - and y -direction, respectively. Moreover, the strain energy density W is given by,

$$W = \int_0^{\epsilon_{ij}} \sigma_{ij} d\epsilon_{ij}. \quad (2.11)$$

When path independency applies, alternate integration contours, with coincident start and end points gives the same value of the J -integral. This holds if the embedded domain of the integration contours fulfils the following requirements [29, 30]:

1. Quasi-static conditions prevail without any body forces present.
2. The material is homogenous in the x -direction. That is, W does not contain any explicit dependence of the x -coordinate.
3. The domain does not encircle a singularity. These are objects that change the energy of the body if the objects position is changed. That is, features such as holes, free edges and concentrated loads are considered singularities.
4. a) The solid is elastic or b) for an elastic or inelastic material when steady state crack propagation occurs.

Here an elastic solid refers to that W exhibits the properties of a potential function. That is, the stress components are explicitly determined by,

$$\sigma_{ij} = \frac{\partial W}{\partial \epsilon_{ij}}. \quad (2.12)$$

This is also known as hyper-elasticity. One central concept in using the J -integral is that inelastic deformation is analysed as being non-linear elastic. That is, condition 4a does not imply that the material must be strictly elastic. Path-independency may apply for inelastic materials during monotonic loading if a function W can be defined so that the stresses are given by Eq. (2.12). A range of inelastic constitutive laws obey Eq. (2.12) during monotonic loading, cf. [31] and [32]. In [33], the authors utilize this in their studies on ductile fracture using a CZM. Thus, the method requires that unloading from an inelastic state does not occur that reveals the difference between non-linear elasticity and inelasticity. Such unloading may be present even if the remote loads are applied monotonically, e.g. in the plastically deformed wake of a growing crack [33].

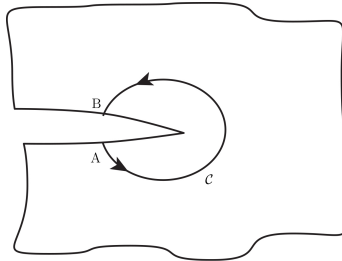


Figure 2.3: Illustration of integration contour, C starting in point A and ending in point B.

The path independency when conditions 1-4a are satisfied is proved in [28]. However, a short discussion is given here for completeness. Path-independency is demonstrated by

showing that the J -integral is zero when evaluated along any closed integration path, \mathcal{C} , that does not encircle any singularity. Equation (2.10) is converted to an area integral by using Cauchy's relation $T_i = \sigma_{ij}n_j$ and employing the divergence theorem,

$$J = \int_A \left(\frac{\partial W}{\partial x} - \frac{\partial}{\partial x_j} \left(\sigma_{ij} \frac{\partial u_i}{\partial x} \right) \right) dx dy, \quad (2.13)$$

where A denotes the domain embedded by the closed contour \mathcal{C} . By utilizing a combination of basic continuum mechanical relations, it is shown that the integrand vanishes if conditions 1-4a are satisfied. With the assumption that conditions 2 and 4a are fulfilled, i.e. Eq. (2.12) holds, the first equality is obtained

$$\frac{\partial W}{\partial x} = \frac{\partial W}{\partial \epsilon_{ij}} \frac{\partial \epsilon_{ij}}{\partial x} = \sigma_{ij} \frac{1}{2} \left(\frac{\partial}{\partial x} \frac{\partial u_i}{\partial x_j} + \frac{\partial}{\partial x} \frac{\partial u_j}{\partial x_i} \right) = \sigma_{ij} \frac{\partial}{\partial x_j} \left(\frac{\partial u_i}{\partial x} \right). \quad (2.14)$$

The second equality is obtained by using the strain-displacement relation, i.e. $\epsilon_{ij} = (\partial u_i / \partial x_j + \partial u_j / \partial x_i) / 2$, from which the right hand side is obtained by utilizing symmetry of the stress tensor, i.e. $\sigma_{ij} = \sigma_{ji}$. Finally, by utilizing static equilibrium $\sigma_{ij,j} = 0$, i.e. assuming condition 1, σ_{ij} can be moved inside the parenthesis. Thus, the integrand of Eq. (2.13) vanishes if conditions 1-4a prevail and the path-independency is shown.

When integration path independency applies, the J -integral evaluated along an arbitrary contour around a crack tip gives the ERR [30]. More specifically, with an arbitrary integration contour that starts in point A and ends in point B as indicated in Fig. 2.3 and the x -direction denoting the orientation of the crack, then $G = J$. In this extended summary, G denotes the ERR with no assumption of applicability of LEFM in line with [30, 29]. In situations when the LEFM assumption is inappropriate Eqs. (2.2, 2.8, 2.9) are not valid². However, in [30], it is shown that although the J -integral is generally path dependent if conditions 1-4 are violated, the J -integral is equal to G when \mathcal{C} is confined to the crack tip, i.e.

$$G = J_{\mathcal{C}} \quad \text{when } \mathcal{C} \rightarrow 0 \quad (2.15)$$

where, $J_{\mathcal{C}}$ denotes the value of J evaluated along an integration path \mathcal{C} shrunk to the crack tip.

The fact that the J -integral gives the ERR is shown in [30] both for the case when path-independency applies and is violated. For the latter case, this result is demonstrated for an integration path \mathcal{C} confined to the crack tip as stated in Eq. (2.15). However, when conditions 1-4a are fulfilled this may be demonstrated using a similar set of equations as used for the proof presented above. This is derived in detail in [34] and the main steps is presented here.

In quasi-static conditions with no body forces present, the potential energy per unit width of the body is given by.

$$\Pi = \int_A W dA - \int_{\mathcal{C}} T_i u_i d\mathcal{C}, \quad (2.16)$$

²In paper C, an additional variable \mathcal{G} is introduced that denotes the ERR obtained from the local field. This is done to differ between the ERR and the apparent ERR obtained from the external loads assuming that LEFM applies.

where A and \mathcal{C} is the area and the outer boundary of the domain. Then the change of potential energy due to a virtual extension of the crack tip becomes,

$$\frac{d\Pi}{da} = \int_A \frac{dW}{da} dA - \int_{\mathcal{C}} T_i \frac{du_i}{da} d\mathcal{C} \quad (2.17)$$

By attaching the coordinate system to the crack tip one obtains,

$$\frac{d}{da} = \frac{\partial}{\partial a} + \frac{\partial x}{\partial a} \frac{\partial}{\partial x} = \frac{\partial}{\partial a} - \frac{\partial}{\partial x} \quad (2.18)$$

since $\partial x/\partial a = -1$. Thus, Eq (2.17) is reformulated as,

$$\frac{d\Pi}{da} = \int_A \left(\frac{\partial W}{\partial a} - \frac{\partial W}{\partial x} \right) dA - \int_{\mathcal{C}} T_i \left(\frac{\partial u_i}{\partial a} - \frac{\partial u_i}{\partial x} \right) d\mathcal{C} \quad (2.19)$$

If conditions 2 and 4a is fulfilled then, analogous to Eq. (2.14), the first term of the first integrand can be formulated as

$$\frac{\partial W}{\partial a} = \frac{\partial W}{\partial \epsilon_{ij}} \frac{\partial \epsilon_{ij}}{\partial a} = \sigma_{ij} \frac{\partial}{\partial x_j} \left(\frac{\partial u_i}{\partial a} \right). \quad (2.20)$$

By the divergence theorem, the first term of the first integral cancels out the first term of the second integral in Eq (2.19). Thus, the remaining of Eq (2.19) reads:

$$\frac{d\Pi}{da} = \int_{\mathcal{C}} T_i \frac{\partial u_i}{\partial x} d\mathcal{C} - \int_A \frac{\partial W}{\partial x} dA \quad (2.21)$$

By using the divergence theorem on the second term we obtain,

$$-\frac{d\Pi}{da} = \int_{\mathcal{C}} \left(W dy - T_i \frac{\partial u_i}{\partial x} d\mathcal{C} \right), \quad (2.22)$$

Thus, when conditions 1-4a are fulfilled, the J -integral evaluated around the crack tip is equal to the energy release rate, G .

The J -integral is a key concept in the cohesive modelling of fracture. Moreover, the conditions for path-independency of the J -integral requires special attention when mixed mode fracture is studied using the CZM. These topics are further discussed in section 3.2.

3 The cohesive zone model

In a LEFM analysis of crack growth, the FPZ is idealized to a mathematical point at the crack tip. Thus, LEFM is suitable when fracture is to be analysed from a pre-existing crack and the size of the FPZ is negligible in comparison with other geometric length scales. However, in other situations a more complete model of the fracture process is required that reflects the nonlinear mechanisms within the FPZ. A candidate to achieve this is offered by the CZM. All inelastic mechanisms acting within the FPZ are lumped into a surface in a 3D analysis or a line in a 2D analysis denoted the cohesive zone in the

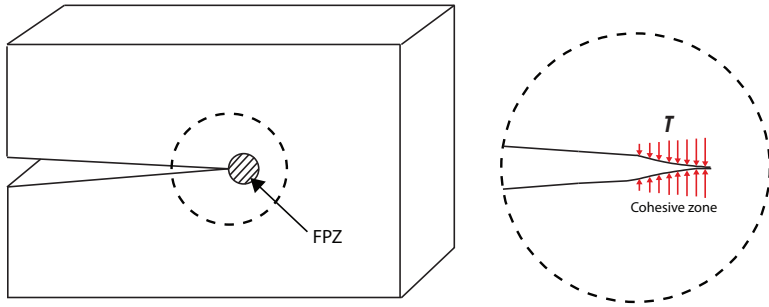


Figure 3.1: Schematic illustration of the cohesive zone representation of the fracture process. All inelastic processes are lumped into a cohesive zone heading a crack tip where the cohesive traction \mathbf{T} holds the cohesive surfaces together.

following, cf. Fig 3.1. Within the cohesive zone, the upper and lower crack surfaces are held together by a cohesive traction, \mathbf{T} , that depends on the separation of the surfaces, δ . For simplicity, the two-dimensional case is discussed in the following. The components of δ consists of the normal separation, w , and the shear separation, v , cf. Fig 3.2a. The conjugated stress components of \mathbf{T} are the normal stress, σ and the shear stress, τ . In the three-dimensional case, one additional shear component that acts out-of-plane is introduced.

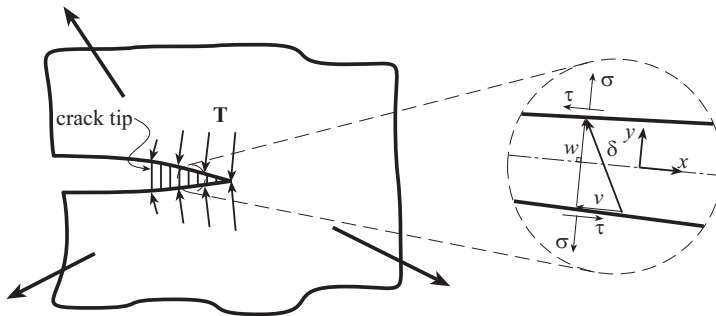


Figure 3.2: *Left*: The definition of the position of the crack tip differs among authors. Throughout this thesis, the crack tip is considered to be situated at the left end of the cohesive zone. *Right*: Orthogonal components of the cohesive traction vector and separation vector.

The response within the cohesive zone is governed by a cohesive law that describes the mathematical relation between \mathbf{T} and δ . A cohesive law for the case of pure mode I loading is illustrated in Fig 3.3a. Initiation of inelasticity is diagnosed when σ reaches the cohesive

strength σ_0 . Beyond this point, the cohesive stress decreases and eventually vanishes indicating the formation of new crack surface. In Fig 3.3a, a perfect bond between the crack surfaces is assumed before σ_0 is reached. However, in most numerical applications, the cohesive law includes an initial part with a finite stiffness, cf. Fig 3.3b, to cope with displacement based finite element analysis. It should also be noted that a finite stiffness sometimes is appropriate and from one point-of-view expected. For example, when the cohesive zone represents a material volume, e.g. an adhesive layer or a resin rich interface in-between plies and not only the inelastic processes within the FPZ.

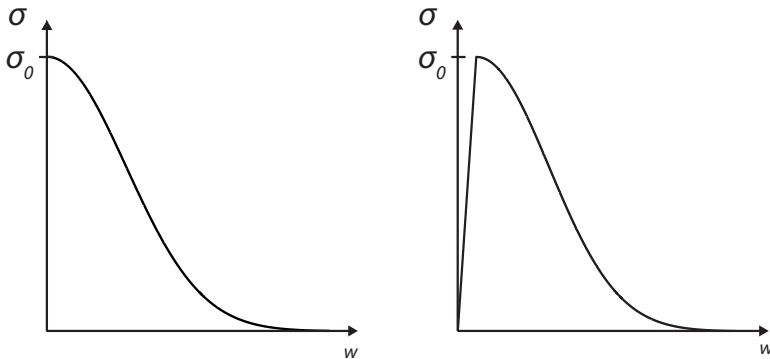


Figure 3.3: Traction-separation relation for mode I loading. a) Initially rigid response. b) Initially linear response.

Cohesive laws relate stresses to separations. Thus, an energy based propagation criterion inherent to fracture mechanics principles is included automatically. The total area under the mode I curve represents the work required by the normal stress to produce mode I fracture. This is denoted the mode I cohesive fracture energy, Γ_I and the mode II counterpart is denoted Γ_{II} ,

$$\Gamma_I = \int_0^\infty \sigma dw|_{v=0}, \quad \Gamma_{II} = \int_0^\infty \tau dv|_{w=0} \quad (3.1)$$

Generally, the cohesive fracture energy Γ is given by,

$$\Gamma = \int_0^\infty \sigma dw + \int_0^\infty \tau dv \quad (3.2)$$

that may depend on the specific loading history. Furthermore, at an instant of separation, the work done by the normal and shear stress ϕ is defined by

$$\phi = \phi_I + \phi_{II} \quad \text{where} \quad \phi_I = \int_0^w \sigma d\tilde{w}, \quad \phi_{II} = \int_0^v \tau d\tilde{v}, \quad (3.3)$$

At the location of a crack tip, ϕ and Γ represent the ERR and the fracture energy,

respectively. Some aspects on the formulation of the evolution of ϕ during monotonic mixed mode loading are discussed in section 3.1.

As pointed out and exemplified in [35], a major benefit of the CZM is the wide range of applicability. This is enabled since the CZM incorporates both a damage initiation criterion and an energy based propagation criterion. Stress-based models are inappropriate when fracture emerges from the location of a stress singularity and LEFM based methods requires an initial crack. These two restrictions are by-passed with the CZM. Thus, the CZM may be successfully calibrated to model fracture in situations where stress-based models or LEFM-based methods or possibly both may be invalid. A more detailed discussion of this is given in section 3.3.

The CZM:s used today stems from the pioneering work of Barenblatt [36] and Dugdale [37]. The introduction of cohesive forces acting ahead of the crack was mainly motivated by the desire to remove the crack tip singularity given by an elastic stress analysis. Barenblatt was focusing on the analysis of the fracture process in a perfectly brittle material by relating the crack resistance to the interatomic binding energy. The cohesive forces between the crack surfaces were assumed to be acting within a small region ahead of the crack tip. Dugdale was using a CZM denoted the strip yield model where the cohesive stress is constant within the complete cohesive zone to estimate the plastic zone size in metals near the crack tip. Later, a CZM known as the fictitious crack model developed by Hillerborg was used to study crack growth in concrete [38]. This model was used as a constitutive property of concrete and was an important extension of the previous work in [36, 37] since a crack was allowed to nucleate and propagate anywhere in the material. Thus, prediction of fracture in initially virgin materials was enabled.

The CZM was first introduced in a finite element context by Needleman [39] to study void nucleation between particles and matrix. Since then, cohesive finite elements have been used to predict fracture in e.g. adhesively bonded joints [40], metals [33] and bi-material interfaces [41]. Delamination in CFRP was first modelled using cohesive elements in the early 1990's, cf. [42, 43, 44]. In addition to delamination problems, cohesive elements have been used to model a variety of failure modes in CFRP at different length scales ranging from debonding of fibre and matrix to macroscopic in-plane failure, cf. the relatively recent review given by Wisnom [35]. Cohesive elements were implemented in version 6.5 of Abaqus and are nowadays available in most commercial finite element softwares.

A drawback with modelling crack growth using traditional cohesive elements is that the crack path must be specified beforehand. However, for e.g. delamination of laminated composites this is not a severe limitation since the crack propagation is restricted to the interfaces between plies [35].

It should however be noted that delamination propagation in CFRP often occurs with some kind of toughening mechanism present, usually in the form of cross-over fibres in the wake of the crack. The increasing resistance during crack growth can be reflected by the cohesive law, cf. [45].

3.1 Types of cohesive laws

Since the introduction of the CZM into FE-codes, numerous cohesive law formulations have been proposed. Most early cohesive law formulations were intended for predicting pure mode fracture or at least when one mode of deformation is very dominating over the other. Cohesive laws of varying softening responses may be categorised as polynomial [46], piece-wise linear [33], exponential [41] and rigid linear [47], cf. [48]. However, interface fracture such as delamination in CFRP usually occurs under mixed mode conditions, cf. section 4.3. Although the mixed mode cohesive law formulations presented in the literature differ in many aspects, especially one fundamental feature enables a separation of the cohesive laws into two groups: potential-based and non-potential-based cohesive laws. In the continuation of this chapter, the discussion is restricted to monotonically increasing separation of the cohesive zone.

Potential-based cohesive laws were first introduced by Needleman [39] and refers to cohesive laws that are derived from a potential function. That is, a function $\Phi(w, v)$ exists that acts as a potential to the cohesive stresses,

$$\sigma = \frac{\partial \Phi}{\partial w} \quad \tau = \frac{\partial \Phi}{\partial v}. \quad (3.4)$$

Integration of both expressions gives

$$\int_0^w \sigma d\tilde{w} = \Phi(w, v) + I_1(v) \quad \int_0^v \tau d\tilde{v} = \Phi(w, v) + I_2(w). \quad (3.5)$$

Thus, by identification of terms the potential function, $\Phi(w, v)$, is given by

$$\Phi(w, v) = \int_0^w \sigma d\tilde{w} + \int_0^v \tau d\tilde{v}, \quad (3.6)$$

That is, $\Phi(w, v)$ is the accumulated area beneath the two curves $\sigma - w$ and $\tau - v$, i.e. $\Phi(w, v) = \phi(w, v)$, cf. Eq (3.3). Thus, for potential-based cohesive laws, both the cohesive stresses, σ, τ , and work performed by the stresses, ϕ , are explicitly given by the current state of separation, i.e. independent of the previous separation history. Potential-based cohesive laws are therefore often referred to as separation path independent cohesive laws. As discussed in [49], uncoupled laws, e.g. [50], constitute a subfamily of potential-based cohesive laws. For such laws, the normal stress only depends on the normal separation and vice versa. That is, mixed mode fracture requires that both $\phi_I = \Gamma_I$ and $\phi_{II} = \Gamma_{II}$ are reached unless a sudden loss of cohesive stress is enforced by the fracture criterion. In papers B-C, a special type of cohesive law is utilized for the modelling of mixed mode fracture denoted initiation-driven cohesive law. For this cohesive law, the properties of the cohesive law are set by conditions at the crack tip at the onset of non-linear deformation. This law exhibits the properties of a potential-based cohesive law during monotonic loading. However, the formulation depends on the conditions at onset of non-linear response and therefore cannot be described by Eq. 3.4.

A number of potential-based cohesive laws have been presented in the literature, e.g. [39, 51, 41, 52, 53, 54]. An important difference between these cohesive laws is

whether or not the cohesive fracture energy, Γ , is independent of the mode mix, e.g. [39, 51] or dependent on the mode mix, e.g. [41, 53]. The ability to calibrate a mode dependent fracture criterion is important in the modelling of many interface fractures e.g. delamination, cf. section 4.3. However, it has been reported that potential-based cohesive laws that allows for a mode dependent Γ may be associated with features that can be considered to be unphysical. In [55, 56], comprehensive reviews are given on this topic. For example, the authors notice repulsive normal stresses under mixed mode loading and that mixed mode failure cannot be modelled by a simultaneous loss of normal and shear stress. In [48], similar results are reported for the commonly used cohesive law by Xu and Needleman [41] when a mode dependent Γ is used.

Cohesive laws that are not formulated from a potential function, i.e. non-potential-based, are also frequently used in the literature. Such cohesive laws are often formulated by explicit functions, $\sigma(w, v)$ and $\tau(w, v)$, e.g. [57, 58, 59, 60, 48]. In [49], the authors show that these laws cannot in general be derived from a potential function unless very restricted conditions are fulfilled. That is, ϕ is generally depended on the loading history. These laws are referred to as stress-based cohesive laws in papers B-C.

Incremental cohesive laws based on plasticity and damage have also been presented, e.g. [61], where neither of σ, τ and ϕ are explicitly dependent on the state of separation.

3.2 Cohesive zones and the J -integral

The existence of a potential function that governs the cohesive law plays an important role in the cohesive modelling of fracture. This is realized by the derivation of G following [30, 29]. To this end, the J -integral is evaluated along a contour \mathcal{C} confined to the crack tip as shown in Fig. 3.4,

$$G = \lim_{\mathcal{C} \rightarrow 0} J_{\mathcal{C}} = \int_{\mathcal{C}} W dy = \left(\int_0^w \sigma d\tilde{w} + \int_0^v \tau d\tilde{v} \right)_{x=0} \quad (3.7)$$

where the subscript $x = 0$ refers to the location of the crack tip. Applying Eq. (3.7) does not require the conditions for path-independency of the J -integral to be fulfilled, i.e. a potential-based cohesive law is not assumed. Thus, the work performed by the cohesive stresses at the crack tip, ϕ^{tip} , represent the ERR, cf. Eq. (3.3). This result was derived in [45] and [62]. In [45], the authors evaluate the J -integral along an integration path that encircles the cohesive zone, cf. Fig. 3.5. In that case, only the second term of the J -integral is nonzero, cf. Eq. (2.10).

The major benefit of potential-based cohesive laws is that path-independency of the J -integral may be applicable provided that the requirements are satisfied also for the surrounding body of interest. This is illustrated in Fig. 3.6 where a fracture mechanical specimen with a cohesive zone assumed ahead of the crack tip is depicted. Evaluating the J -integral close to the crack tip gives the right hand side of Eq. (3.7). With a cohesive zone governed by a potential and an elastic bulk, condition 4a stated in section 2.2 is fulfilled. Furthermore, if conditions 1-3 are fulfilled, then path-independency applies. Thus, all counter-clockwise integration contours about the crack tip give the same value of J , i.e. the ERR. That is, there is a direct relation between the cohesive stresses acting

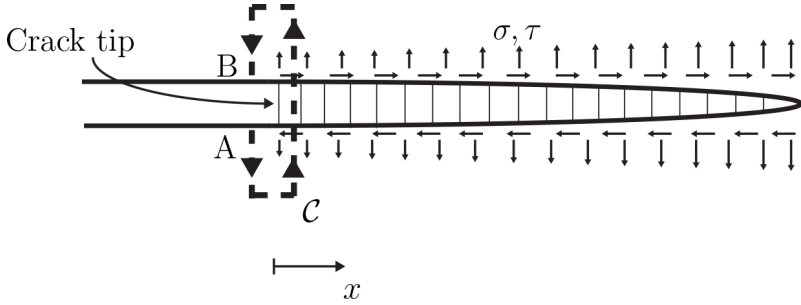


Figure 3.4: Counter-clockwise integration contour \mathcal{C} confined to the crack tip taken from the lower point of the crack tip, A, to the upper point of the crack-tip, B. For visibility, the cohesive zone has a finite height and \mathcal{C} is sketched outside the cohesive zone.

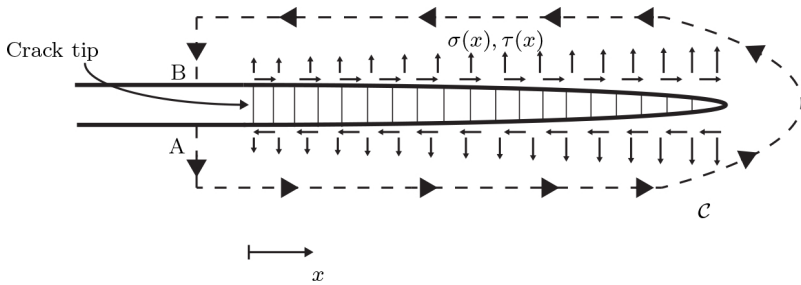


Figure 3.5: Counter-clockwise integration contour \mathcal{C} about the cohesive zone taken from the lower point of the crack tip, A, to the upper point of the crack-tip, B. For visibility, the cohesive zone has a finite height and \mathcal{C} is sketched outside the cohesive zone.

at the crack tip and J as evaluated along the outer boundaries of the specimen, cf. the contour \mathcal{C}' indicated in Fig. 3.6. For many test specimens, this enables a straightforward measurement of ERR from the applied loading and displacements. Moreover, when SSY conditions prevail, J as evaluated along contour \mathcal{C}' may be expressed by using the LEFM techniques discussed in section 2.1. This is frequently utilized in papers A-C.



Figure 3.6: Illustration of the outer integration contour \mathcal{C}' .

The relation between cohesive laws and the J -integral has been used to determine cohesive laws associated with fracture of adhesive joints and fibre bridging in CFRP.

Some significant contributions are given in section 3.3. Noteworthy is that for pure mode monotonic loading, all cohesive laws may be described by Eq. (3.4). Thus, path-independency of the J -integral applies for pure mode loading given that the surrounding bulk fulfils the requirements.

For cohesive laws that is non-potential-based, the conditions for path-independency of the J -integral is violated. That is, a relation between the cohesive stresses at the crack tip and the external loading cannot in general be established. This can be demonstrated by studying the closed integration path depicted in Fig. 3.7. The closed path encircles the cohesive zone with the left end just to the right of the crack tip. Since the cohesive zone is not governed by a potential function, Eq. (2.14) is invalid. Thus, according to Eq. (2.13), J for the closed path is generally not zero if the cohesive law is non-potential-based. This implies path-dependence of J when evaluated for a path starting at the lower crack surface and ending at the upper. However, under very specific circumstances exceptions to this may be encountered. In paper C, it is demonstrated that non-potential based cohesive law can be formulated such that potential-based properties are exhibited under mixed mode SSY conditions.

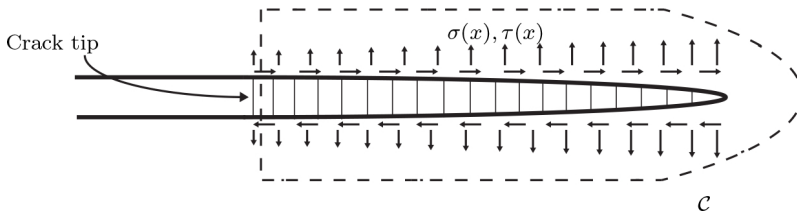


Figure 3.7: Illustration of a closed integration contour surrounding the cohesive zone.

It should also be noted that, as long as the deformation of the bulk material surrounding the cohesive zone can be associated with a potential function, the contour encircling the cohesive zone in Fig. 3.5 and C' shown in Fig. 3.6 or any integration path in between them will give the same result. This is realized by noting that the enclosed domain by two such paths fulfil the requirements for path-independency. However, if the cohesive law is non-potential-based, none of them give the right hand side of Eq. (3.7).

3.3 Influence of cohesive parameters

In this thesis, experimental and numerical work are combined for a detailed determination of cohesive laws associated with delamination nucleation, cf. papers A-B, and longitudinal compressive failure, cf. paper D. Often when cohesive elements are used to model fracture, the solution is insensitive on the precise formulation of the cohesive law. However, the cohesive laws determined in this thesis are intended to model these failure mechanisms in aeronautical CFRP structures including the nucleation of cracks in a defect-free material or from a small-scale defect. An important step for safe design is to evaluate the effect of defects that are on the threshold of detectability during a visual inspection. Such defects may escape detection and reduce the load carrying capacity of the component.

In such cases, the FPZ cannot be considered to be of negligible size compared to other relevant dimensions. Under such conditions, a more detailed model of the fracture process is required and the predicted response may be affected by all details of the cohesive law.

As previously discussed, a large benefit of the CZM is its versatility to allow for modelling of crack growth in a wide variety of situations. Depending on the loading conditions for which fracture is to be modelled, different parameters and features of the cohesive influence the results. In the extreme case of a cohesive zone subjected to homogenous stress, the stress initiation criterion single-handedly dictates the fracture load. For mixed mode conditions, initiation is usually modelled using a criterion that takes the interaction of the cohesive stresses into account. The most commonly used interaction criterion is the quadratic stress criterion proposed by Ye in [63] although several alternatives have been proposed, e.g. [61, 59]. In the opposite extreme situation, crack growth is modelled from a pre-existing crack and the fully developed cohesive zone is of negligible size compared to other geometric dimensions. Under such circumstances, the cohesive fracture energy is the only parameter of importance. For pure mode I and II loading, the fracture load is completely dictated by Γ_I and Γ_{II} , respectively in line with LEFM. However, care must be taken to this statement in the general mixed mode case. As discussed in the previous section, even when LEFM applies, the fracture load cannot in general be related to the cohesive fracture energy given by the cohesive stress-separation history at the crack tip. This is only possible if the cohesive law is derived from a potential function.

As the size of the fully developed cohesive zone increases relative to other relevant geometric lengths, additional details of the cohesive formulation influence the predictions, cf. e.g. [64, 35, 29]. It is often suggested that the cohesive fracture energy and the cohesive strength, are the only parameters of importance. This holds in many situations and has been demonstrated for e.g. ductile fracture by Hutchinson and Evans in [65]. A comprehensive discussion on this topic is given in e.g. [64]. In their studies, the authors conclude that additional details of the cohesive law may strongly influence the results. Latterly, further studies on the effect of individual cohesive parameters have been reported in e.g. [66, 50, 64, 67, 68]. Many of these results suggest that all aspects of the cohesive law should be chosen with care and sometimes details that usually are considered unimportant substantially influence the macroscopic behaviour. A restriction is however necessary for the case of mixed mode loading and the reported effects of cohesive parameters. It is complicated and sometimes impossible to relate variations of the results to one single feature of the cohesive law. For example, changing the shape of the cohesive law may also affect the cohesive fracture energy obtained. However, pure mode loading allows for studies of the influence of individual features in isolation.

Usually, the effect of three features of the cohesive law formulation are examined, i.e. the cohesive strength, the cohesive fracture energy and the shape of the softening function. The latter is often considered unimportant and therefore chosen as simple as possible with the bilinear softening model being the most commonly used. However, several studies have been presented where the observations contradict this assumption, cf. [69, 70, 71, 72, 64, 73, 74, 75]. This implies that the effect of the shape of the cohesive law may be underestimated in numerical analysis of e.g. delamination nucleation.

In references [69, 70, 71], the authors investigate the response when the cohesive

fracture energy and cohesive strength is kept fixed while varying the shape of the softening function. For example, in [69] it is demonstrated that both the critical load and the stability of the load displacement curve in simulations of the short beam shear test are strongly affected. Moreover, in [70], the authors present simulations of three point bending specimens and curved specimens subjected to bending moments. Cohesive elements are inserted at all locations susceptible to delamination. The specimens contain discontinuous plies to simulate a ply drop. Both perfectly plastic and linear softening responses are used and successful prediction of the locations of delaminations is reported for both formulations. Also, the failure loads are accurately predicted for the straight specimens for both formulations. However, for the curved specimens, the failure load is successfully predicted with the softening law while the perfectly plastic response gives un-conservative results. Furthermore, in [71], free edge delamination in laminates of various stacking sequences subjected to uniaxial tension are simulated. Different failure loads are obtained, although the effect is moderate, when using linear or exponential softening.

In [72], the authors calibrate the mode I cohesive law for fracture in various materials using notched and un-notched three-point bending specimens. For specimens with a short initial crack and for un-cracked specimens, the mode I strength and the initial slope of the softening curves dictate the global response. That is, the peak load occurs after the cohesive strength is reached but before the cohesive zone is fully developed. With a suitable mode I strength and initial slope of the softening curve, the authors also accurately predict the load vs. notch opening displacement curves for beams with U-shaped notches made of concrete, PMMA and steel. In [64, 73], it is demonstrated that for more brittle decohesion, the shape of the traction-separation relation plays a decisive role, sometimes even more important than the cohesive strength.

The shape of the cohesive law may be important when a dissipative material is surrounding the crack tip. In [64, 74], this is shown for a thin slice push-out test for a composite system. Interface failure between fibre and matrix is modelled using an elastic response for the fibre and an elasto-plastic response for the matrix. The simulated response is completely different for various shapes of the mode II softening function.

These observations indicate that detailed formulation of the cohesive law may be important and it should be determined for each specific situation. Therefore, it is desirable to determine cohesive laws based on experimental measurements. Experimental methods to extract cohesive laws from physical testing have been presented for adhesive joints, in e.g. [76, 40, 77, 78, 79, 80, 62, 81] and for crack bridging in composites in e.g. [82, 45, 83, 84, 85]. In these works, the authors utilize the J -integral and its relation to the CZM as briefly discussed in the previous section. Recently, in [86], Jalalvand et al present an alternate technique to extract the mode II cohesive law associated with delamination in CFRP. In-situ measurements of the mode II deformation of the resin rich interface is continuously measured and inserted into the in-plane shear constitutive relation.

3.4 Element size requirements

One large benefit of using cohesive elements is the ability to provide relatively mesh independent results. The problem of highly mesh dependent results in the presence of a stress singularity is often encountered when continuum damage models are used, e.g. [87]. The number of cohesive elements required for an accurate modelling of the fracture process is discussed in a number of articles, e.g. [88, 89]. A minimum of 2-3 elements within a fully developed cohesive zone is usually recommended. However, in [90] more than 10 elements and in [91] more than 15 elements are recommended.

Various analytical models to estimate the fully developed cohesive zone lengths and thereby the required element size are commonly utilized. These models are discussed in [89]. Usually, they are based on the model proposed by Hillerborg in [38] that approximates the cohesive zone length for a semi-infinite crack in an infinite isotropic solid subjected to remote mode I loading,

$$\zeta = \frac{\bar{E}\Gamma_1}{\sigma_0^2}. \quad (3.8)$$

Here, \bar{E} is the plane stress or plane strain elastic modulus of the bulk. For orthotropic materials that are transversely isotropic, \bar{E} denotes the transverse elastic modulus [89].

For delamination of CFRP, typical values of the mode I interlaminar strength and fracture energy gives rather small cohesive zones. The requirement of mesh refinement is therefore troublesome in larger scale structural simulations. Techniques to allow for coarser meshes have been proposed, cf. [89]. Comparing ζ with other characteristic geometrical lengths gives an indication whether or not the results are sensitive to the cohesive strength and additional details of the cohesive law [89, 50]. When ζ is small, the strength can be reduced while keeping the cohesive fracture energy constant. Thus, larger cohesive zones are obtained and thereby a coarser mesh may be used without affecting the structural response. In [89], guidelines are given on the selection of appropriate cohesive parameters. Of course, if the cohesive zone is enlarged too far, the structural response may be affected and become sensitive to individual cohesive parameters.

In papers A-C, more than 100 cohesive elements are placed within the fully developed cohesive zone. This is obviously an excessively high discretisation for most applications, e.g. to obtain converging fracture loads. However, the complete decohesion process is studied and detailed modelling is required also in the initial stages of the simulations.

3.5 Initial stiffnesses

When cohesive elements of zero height are inserted in into a surrounding continuum with stiffness properties according to macroscopic bulk data, no cohesive opening should occur prior to the onset of damage. For this purpose, the authors in [47] implement an initially rigid cohesive model into a FE-software. This is carried out by automatically inserting cohesive elements into the element mesh once the stress reaches the initiation criterion. However, the use of cohesive elements in a traditional FE-code requires an initial finite stiffness. The separation that occurs prior to initiation of damage is limited by choosing

a very high elastic stiffness of the cohesive element. In [89], it is suggested that a lower bound for the initial stiffness can be determined by $K = \alpha E_3/t$, where E_3 is the through the thickness Young's modulus and t is the thickness of the adjacent continuum. The authors suggest a minimum value of $\alpha \geq 50$ that results in a global stiffness loss less than 2 %.

However, as demonstrated in [92], excessive initial stiffnesses may result in spurious stress oscillations that precludes solution convergence. This is demonstrated in papers B-C in the simulation of mixed mode fracture. During linear elastic response, the mode partitioning at the crack tip should agree with LEFM, i.e. $\phi_I = G_I$ and $\phi_{II} = G_{II}$. It is however noted that this is only achieved when initial stiffnesses below a certain limit is used. This limit depends on the stiffness of the bulk and size of the continuum elements adjacent to the cohesive zone. The correlation between mesh sizing and allowable initial stiffness is however weak and substantial mesh refinement is required to allow for a somewhat increased allowable stiffness. Moreover, for simulation of delamination in CFRP, it is noted that choosing the initial stiffnesses based on resin moduli and a typical thickness of the resin-rich interface gives an order of magnitude higher initial stiffness than allowed.

3.6 Cohesive zones and LEFM

When the cohesive zone is small compared to other geometrical lengths the predicted results should conform to the predictions given by LEFM. More specifically, it is desirable that the model reproduces the experimental data obtained from fracture mechanical tests. In [50] it is argued that, under such conditions, the mode partitioning should agree with the predictions of LEFM, i.e. $\phi_I = G_I$ and $\phi_{II} = G_{II}$. With this capability at hand, calibration of the cohesive is straight forward and LEFM results are obtained whenever SSY conditions are present. However, in [59, 93, 66] it is demonstrated that this is generally not the case in the simulation of delamination. Instead, the mode partition has shown to vary during non-linear response in the cohesive zone. These studies show a propensity towards normal separation is initiated at the onset of non-linear response in the cohesive zone. Such behaviour makes calibration of the fracture criterion troublesome if LEFM results are used for calibration of the cohesive law.

In [50], it is demonstrated that this behaviour is avoided by using an uncoupled cohesive law. The authors demonstrate that the mode partitioning coincide with LEFM for a wide variety of softening functions provided that the cohesive zones are sufficiently small. For this model, a coupled fracture criterion is used that instantly drops the cohesive traction to zero when a critical state of separation is reached.

3.7 Discussion of the results in paper C

In paper C, the conditions for which coupled cohesive laws are able to conform to LEFM are investigated. It is demonstrated that a constraint is required that relate the cohesive stiffnesses with the elastic stiffnesses of the orthotropic bulk. A second condition is found necessary that concern the formulation of the non-linear response of the cohesive law.

That is, a constant ratio between w and v must imply that ϕ_I and ϕ_{II} are constantly related. This is not possible to achieve with a potential-based cohesive law that possess a mode dependent Γ . It is shown that the initiation-driven and stress-based cohesive laws can fulfill these two conditions and allow for a mode dependent mode mix.

As previously discussed, the use of a non-potential based cohesive laws implies that the J -integral is path dependent. Thus, the cohesive stresses at the crack tip cannot generally be directly related to the remotely applied J . It is however demonstrated that this difficulty can be by-passed during SSY conditions. With both conditions fulfilled, the stress-based cohesive law exhibits the properties of a potential.

4 Delamination

The lack of reinforcement in the through-the-thickness direction makes laminated composites susceptible to delamination. Resin rich interfaces between plies accumulate damage that leads to a complete separation of adjacent plies.

Delamination embedded within the laminate may be difficult to detect during inspection. It must therefore be considered that unnoticed delaminations may exist during service of the component. Moreover, it is widely known that the existence of delaminations, even small ones, may noticeably reduce the strength and stability of the component. For example, under compressive or flexural loading, delaminations have shown to promote micro-buckling in the load-bearing plies leading to catastrophic failure of the laminate [94]. Moreover, delaminations tend to propagate under such loading conditions by buckling of the sub-laminates, i.e. buckling driven delamination [95, 96]. The existence of delaminations must therefore be accounted for already in the design of the structural component [95].

In [10], the critical role of delaminations is also demonstrated for the unnotched tensile strength of multidirectional laminates. Laminates with different stacking sequences are tested, all with the same nominal stiffness and strength according to classical laminate theory (CLT), cf. e.g. [97]. The results show a substantial variation of the laminate strength and the strength predicted by CLT are unconservative for all lay-ups. This is explained by the varying development of matrix cracks and free edge delaminations.

It is therefore important to enable prediction of the loading conditions for which delamination initiates and propagates. Experimental characterisation and modelling of delamination have been topics of intensive research during the four last decades. The research progress has been summarized in useful review articles and books, e.g. [98] that covers the progress during the 1970's and 1980's, [96] that covers the years 1990-2001 with special emphasis on buckling driven delamination and more recently the comprehensive review in [99] on experimental and numerical techniques.

4.1 Sources of delamination

In CLT, the laminate and the individual lamina are assumed to be under the condition of plane stress, i.e. the stress components in the through-the-thickness direction are zero.

Although this is normally a valid assumption, there are circumstances where substantial interlaminar stresses are present and may cause delamination. In Fig. 4.1, common sources of interlaminar stresses are depicted. They correspond to locations of geometric or material discontinuities.

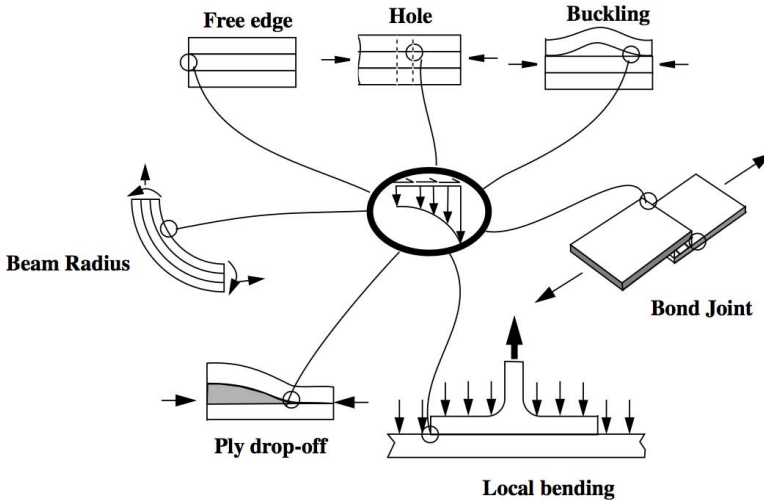


Figure 4.1: Sources of interlaminar stress. Picture: courtesy of professor Tonny Nyman, SAAB Aeronautics/Royal Institute of Technology, Sweden.

Geometric discontinuities are commonly encountered in various engineering applications. For example, internal ply drop-offs are used when a varying thickness of the laminate is desired. Axial loads are transferred to the continuous plies through interlaminar shear stresses. Also curved sections subjected to bending moments are locations where delaminations may occur due to the radial stresses. In the design of advanced composite structures, both curved laminates and varying laminate thicknesses are necessary and may be risk areas for delamination. Studies of delamination growth near ply drop-offs and curved regions are investigated in e.g. [100] and [70]. Moreover, abrupt local discontinuities in the form of manufacturing defects, e.g. matrix cracks, cavities and damaged fibres within the laminate may be trigger points for delamination.

Material discontinuities are present at interfaces between plies of different orientation due to the mismatch of mechanical properties. The adjacent plies have different normal-shear-coupling or Poisson's ratios or possibly both. When bonded, interlaminar shear stresses and sometimes tensile normal stresses are induced at free edges, at holes and notches. Moreover, the varying fibre orientations results in a mismatch of coefficients of thermal and moisture expansion. Thus, the working environment of the material needs to be considered in the design to avoid interlaminar damage growth. Also during curing where the laminate is heated and cooled may generate substantial interlaminar stresses, especially for multidirectional laminates that are curved.

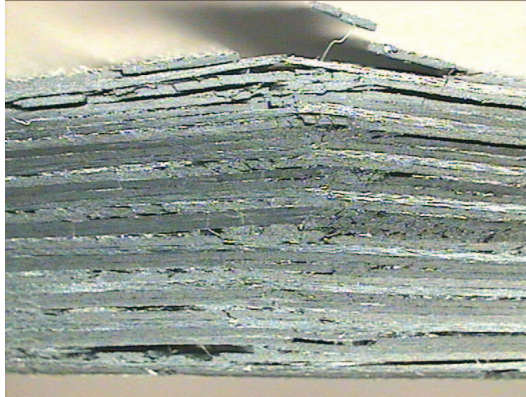


Figure 4.2: Microscope image of an impacted laminate. Accompanied by fibre failures and matrix cracking, multiple delaminations are present. Picture: courtesy of Dr. Sören Nilsson, Swerea SiComp.

Out-of-plane loading is widely recognized as a critical source for delamination. One scenario that is especially important in the aeronautical industry is that CFRPs are prone to delaminate due to impact loads that may occur by e.g. a strike of hail or a tool-drop. Figure 4.2 displays a microscope image of an impacted laminate where multiple delaminations are visible. Since delaminations are known to severely reduce the compressive strength of the laminate, the research community has devoted much effort on the characterisation of the compression after impact strength, e.g. [101].

As highlighted in [35], delamination usually interplays with other failure modes, in particular intralaminar cracking. Because of the low transverse strength, intralaminar cracking can initiate at relatively low loads. These cracks give localized interlaminar stresses that cause delaminations [94]. Delaminations can interact through these matrix cracks and cause catastrophic failure of the laminate.

4.2 In-situ observations of delamination growth

The inelastic mechanisms that take place on the microscopic scale in the delamination process are complicated. Due to the heterogeneity and anisotropic properties of these materials, the fracture processes are conceptually different than usually observed in homogeneous isotropic materials. Important factors that influence the fracture process are for example: the mode of loading, the properties of the matrix material and fibre/matrix adhesion. Moreover, the interfacial resin layer thickness and ply orientation of the adjacent plies have an impact on the microscopic process.

In homogeneous isotropic materials, fracture is often anticipated to take place as a mode I crack, i.e. normal to the principal stress. However, the laminated structure, to a large extent, restricts the nonlinear deformation to the resin layer in-between the adjacent plies that forms the delamination crack. This promotes delamination to nucleate under

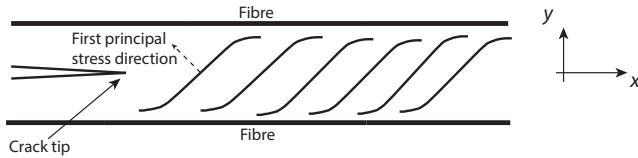


Figure 4.3: Schematic sketch of S-shaped microcracks ahead of the delamination front. Picture re-drawn from [103].

mixed mode conditions and the fracture process is significantly dependent on the mode of loading of the interface.

With relatively brittle resins, the delamination mainly occurs through the formation and coalescence of microcracks in the resin layer and debonding of the fibre/matrix interface. Ahead of the delamination front, a narrow band of microcracks within the resin rich layer is formed. The orientation of the microcracks depends on the mode of loading and tend to orientate perpendicular to direction of the principal stress [102]. This is illustrated in Fig. 4.3.

For mode I loading, the microcracks are approximately oriented parallel to the x - z -plane. As the mode II part of loading increases, the principal stress direction changes and the microcracks are increasingly inclined with respect to the x - z -plane. For mode II loading, cracks orientated approximately 45° to the x - y -plane are formed ahead of the crack tip. If the adjacent fibres are orientated not to different than the x -direction, then propagation of the microcracks into the adjacent ply is prevented [104]. Therefore, as the microcracks reach the fibres they kink and propagate along the fibre matrix interface as shown in Fig. 4.3. A macroscopic crack is eventually created through the coalescence of these S-shaped microcracks at the tensile loaded interface. This process creates cusps or hackles of resin that leaves an apparent rough fracture surface [105, 104]. This sequence of events is observed by the authors in [106] where mixed mode experiments are conducted on a similar material system as studied in papers A-B.

Since mode II fracture occurs via matrix cracks that fail in tension, it is suggested in [105] that G_{IIC} should not be considered as a material parameter.

The length of the fully developed microcrack zones range from tens of microns to about 1 mm [102]. The smallest FPZ:s are found in pure mode I tests and the size increases with the mode II part of the loading. The size of the FPZ is also strongly dependent on the thickness of the resin-rich layer [102]. For CFRP prepregs, resin layers are typically about 10-20 μm thick [102]. However, this thickness varies significantly depending on e.g. ply orientations. In [107], the authors perform mode II tests on unidirectional specimens of a similar material that is studied in paper A-B. The specimens are polished and investigated post fracture in a SEM. A FPZ of 460 μm is identified.

In [104], it is demonstrated that the fracture process is often changed when the adjacent plies have significant dissimilar fibre orientation. For such interfaces, the microcracks may continue into the adjacent ply as shown in Fig. 4.4. Thus, delamination cracks may switch the propagation interface through intralaminar cracking. This mechanism, referred to as delamination migration is discussed in detail in [108]. Delamination migration is one of

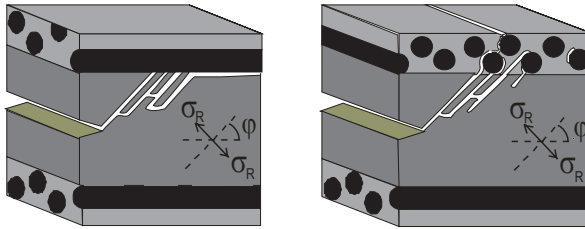


Figure 4.4: Microcracking ahead of the crack tip. *Left*: 0°-0° interface. *Right*: 0°-90° interface. Picture slightly modified from [104].

the sources to the difficulties associated with delamination testing using multidirectional specimens, cf. section 4.3.

Although microcracking is considered as the major failure mechanism for relatively brittle resins, plastic deformation is present as well. In [109], Bradley observes substantial resin strains in localized areas near the crack tip. For mode I, localized resin strains exceeding 10 % are obtained for the relatively brittle composite system AS4/Dow P6. This is significantly higher than obtained by tensile tests of this resin. It is also demonstrated that G_{IC} for brittle composite systems are substantially larger than the neat resin mode I fracture energies. This is mainly explained by the development of a longer FZP:s in the composite. For mode II tests on the brittle composite AS4/3501-6, a surprisingly high shear strain of 74 % is measured. It is however noted that the measured deformation mainly consists of microcracking and cusp formation rather than straining of the resin. Moreover, for brittle matrix materials, G_{IIC} is considerably larger than G_{IC} . The longer FPZ of microcracking found in mode II tests are considered the main reason for this.

Studies have been presented that suggest that the plastic zone ahead of the crack tip cannot be considered confined to the resin-rich layer. In [110], Olsson gives a comprehensive review on factors that influence the G_C in composites, e.g. the plastic yield zone ahead of the crack tip. As cited in [110], the plastic zone size in a brittle composite subjected to a mode I test was measured by Parker in [111] where the yield zone found in the composite system was about eight times thicker than observed in tests of pure resin.

In [112], the authors conduct micromechanical FE-analyses of the delamination front of a DCB-specimen. The material data used for the simulation describes a significantly more brittle material than the material used in papers A-B. They found that the fibres induced yield zones in the resin in-between the fibres in the adjacent plies. The authors therefore suggest that the presence of fibres can actually increase the size of the yield zone.

For tough matrix materials, the fracture process is conceptually different than observed for brittle matrix materials [109]. The microcracking discussed above does not form and the fracture process is similar for mode I and II loading. Fracture is governed by plastic deformation followed by ductile tearing for both modes and for very tough resins $G_{IC} \simeq G_{IIC}$. It is also demonstrated that increasing G_C of the composite by using a

tougher resin is only effective up till a certain limit. The laminated structure prevents large yield zones to develop and thereby limits the effect of using a very tough resin. Moreover, as discussed in [110], the strength of the matrix/fibre interface may also limit G_C of the composite material.

4.3 Characterisation of delamination resistance

Predictive tools for delamination are usually based on fracture mechanics and therefore require knowledge of G_C . Determination of the interlaminar G_C is normally based on LEFM unless toughening mechanisms that may yield large FPZ:s, such as fibre bridging, are assumed to be present. As discussed in section 4.2, for relatively brittle resins, the fracture process is highly dependent on the mode of loading. Consequently, experimental experience, e.g. [113], show that G_C varies with the mode of loading. Thus, predictive tools require determination of G_C for a range of modes and fracture is predicted as

$$G_I + G_{II} \geq G_C(\Lambda_{\text{glo}}). \quad (4.1)$$

where the mode mix measure $\Lambda_{\text{glo}} = G_{II}/G$ is frequently used. Generally for CFRP:s, G_C takes its minimum value for pure mode I loading and increases as Λ_{glo} increases [104].

In predictive models assuming LEFM, the experimentally obtained G - Λ_{glo} -relation is approximated with a failure criterion. A commonly used criterion for delamination restricted to mode I/II combinations is the BK-criterion [113] given by

$$G_c = G_{Ic} + (G_{IIc} - G_{Ic})\Lambda_{\text{glo}}^\eta \quad (4.2)$$

where η is a curve fitting parameter. Multiple criteria have been proposed in the literature, cf. e.g. [114], where several criteria consider all three modes of loading.

Test methods for the determination of G_C are reviewed in [115], [96] and more recently in [116]. The most adopted tests are the Double Cantilever Beam test (DCB) [117] for mode I, the End Notch Flexure test (ENF) [118, 119] for mode II and the Mixed Mode Bending test (MMB) [120] for mixed mode I/II loading. In the MMB-tests designed by Reeder and Crews [121, 122], mixed mode I/II loading is applied to the specimen through a lever arm. Various mode mixities are conveniently obtained by adjustment of the lever arm length. These tests geometries are shown schematically in Fig 4.5.

Experimental tests are usually conducted on UD specimens even though delamination in real composite components tend to occur between plies of different fibre orientation [104]. Thus, it has been questioned if the experimentally determined G_C is representative for the modelling of delamination [104]. The main reason that unidirectional specimens are used is the large difficulties to achieve true delamination in multidirectional specimens. When the fibre orientations are very different from the longitudinal direction of the specimen, intralaminar matrix cracks tend to develop well before delamination takes place [123]. Moreover, delamination migration and multiple propagation planes contribute to an artificially increased G_C during crack propagation [124, 125]. These mechanisms make the conventional calculation methods for G invalid [123]. It has been demonstrated that delamination tests on multidirectional specimens produce fracture surfaces that are significantly different than observed in real components [96, 104]. Moreover, G_C is strongly

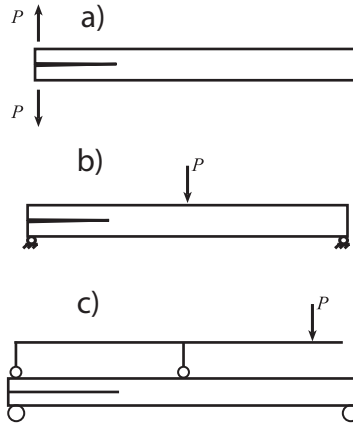


Figure 4.5: a) Double cantilever beam (DCB). b) End notch flexure (ENF). c) Mixed mode bending (MMB).

dependent on the thickness of the resin-rich interface [104]. As discussed in section 4.2, thicker resin layers allows for larger FPZ:s to develop. Thus, the thinner resin layers found in unidirectional specimens may give lower G_C than multidirectional specimens. On the other hand, during crack extension, the thinner resin layers may promote substantially increasing G_C attributed to fibre bridging. In interfaces between aligned plies, fibres tend to nest. Thus, a bridging zone with cross-over fibres is often observed in the wake of the crack during propagation in unidirectional specimens.

The effect of ply orientations on the initiation value of G_C have been experimentally examined. It is often found that G_C is almost unaffected by the ply orientations in mode I loading [126, 104]. For mixed mode and mode II loading, delamination between plies of different orientations results in G_C that are generally higher than obtained with unidirectional laminates, e.g. [127, 128]. In [123], Andersons conducts a comprehensive tests series that includes MMB tests with $0.2 \leq \Lambda_{\text{glo}} \leq 0.8$ on specimens with mismatch angles between plies from 0° to 90° . It is found that G_C generally increase with the mismatch angle of adjacent plies. The effect is substantial for mode II dominated loading but decreases as the mode II part of loading decreases. Thus, it is generally conservative to predict onset of delamination based on G_C obtained in tests on unidirectional specimens.

Related to the influence of the resin layer thickness is the discussion of the manufacturing of the starter crack in delamination tests. Ideally, the initial crack front would consist of a virgin resin-rich layer with the same thickness as found far ahead of the crack front. However, manufacturing of such a starter crack is troublesome. Different methods to produce the starter crack are discussed in the review given by Tay [96]. Usually, the starter crack is formed by placing a Teflon film or an equivalent film between adjacent plies prior to curing of the laminate. It has been demonstrated that a resin pocket may be formed near the tip that influences the measurement of G_C [129]. Fracture of the resin pocket is required before a true delamination crack is formed. This gives an artificial high

value of G_C and unstable crack propagation. The thickness of the resin pocket depends on the thickness of the insert. Thus, the standards of the DCB- and MMB-tests recommend inserts not thicker than $13 \mu\text{m}$ [117, 120].

To circumvent these problems, specimens are commonly pre-cracked beyond the resin pocket. However, it is difficult to obtain a representative delamination front also with pre-cracking. Damage ahead of the crack tip is likely introduced and conservative G_C is therefore promoted, especially in mode II dominated tests [130]. On the other hand, as a result of mode I pre-cracking, bridging fibres behind the crack tip is likely to be present that would increase G_C [131]. In [105], O'Brien discuss the significant difference of G_{IIC} obtained with specimens that are pre-cracked by mode II loading and specimens with inserts only. It is suggested that microcracks are formed ahead of the crack tip during pre-cracking. In the tests, mode II delamination is created by the coalescence of these pre-existing microcracks.

Delamination tests usually display increasing G_c during extension of the crack. For unidirectional specimens, the source of increased resistance is mainly fibre bridging [132, 133]. Substantial bridging zones may develop that makes the LEFM approach invalid, i.e. large scale bridging conditions are present. In [45], mixed mode cohesive laws associated with fibre bridging are measured using the J -integral approach.

4.4 Interlaminar strengths

The interlaminar strengths are substantially lower than the in-plane strength of multidirectional laminates and thereby limiting parameters for safe design of CFRP components. With LEFM based methods, there is no concept of strengths and crack growth is governed by the energy release rates alone. However, to enable prediction of delamination when LEFM is inappropriate, accurate values of the interlaminar strengths are crucial. Both the CZM and damage mechanics based models require the interlaminar strength as input parameters. In the extreme case of homogenous interlaminar stress, the interlaminar strengths single-handily dictates when delamination occurs.

The interlaminar shear and tensile strength are properties that are very difficult to characterise. Therefore, it is common to approximate the interlaminar strengths with the transverse in-plane strengths. There is yet no widely accepted method to measure the in-situ interlaminar strengths that acts on the resin layer between plies.

There are standardized tests for the measurement of the "apparent" interlaminar tensile and shear strength. The term apparent is commonly used due to the fact that these tests produce rather complex stress states. However, the tests are considered to give dominating interlaminar tensile and shear stress, respectively. Thus, the results are considered valid for comparison and as a quality assurance [135, 136].

For measurement of the tensile strength, a curved beam subjected to four-point bending is frequently utilized [135]. The specimens are unidirectional laminates with a 90° out-of-plane bend located at half the span length, cf. Fig. 4.6. The bending moment gives rise to localized interlaminar tensile stress in the curved region. A major drawback with this test is the difficulty to manufacture a curved region of good quality. The local region near the curvature often displays increased porosity and reduced fibre content and

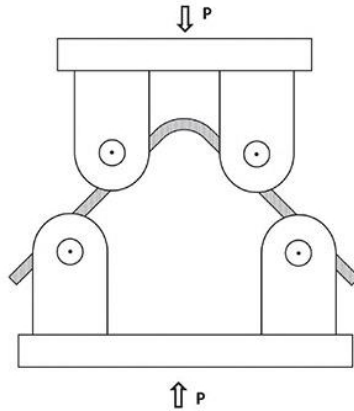


Figure 4.6: Sketch of the curved beam test. Picture from [134].

the tests usually exhibit large scatter [137]. It is thereby questionable if this test generates strengths that are representative for straight laminates.

The most frequently used test method for the shear strength is the short beam shear test [136]. In this test, a straight unnotched unidirectional specimen is subjected to three-point-bending. Interlaminar shear failure is promoted by choosing a low span length/height ratio. The data reduction of this test usually relies on classical beam theory, i.e. a parabolic shear stress distribution along the thickness direction. However the stress states are much more complicated due to stress concentration at the supports and load point, the low span length/height ratio and the neglecting of the nonlinear interlaminar shear response [138, 44].

4.5 Objective and method in paper A and B

The objective of papers A-B is to extract cohesive laws associated with the nucleation of delamination. Paper A deals with mode I and II and paper B extends that study with mixed mode loading. The cohesive law is intended for studying delamination using cohesive finite elements surrounded by a linear elastic continuum modelled with orthotropic finite elements. Thus, the cohesive law represents all elastic and inelastic processes in a material volume at the proximity of the delamination front. These processes are lumped to a cohesive surface, cf. chapter 3. As discussed in section 4.2, these processes are not necessarily confined to the resin-rich layer in-between plies. Thus, the cohesive law represent the behaviour of the resin-rich layer and, to some extent, also the behaviour of the adjacent plies.

Fracture mechanical tests are conducted on unidirectional DCB, ENF and MMB specimens. To avoid bridging fibres in the wake of a growing crack, cf. the study in [139], one ply adjacent to the artificial delamination is angled 5° . The starter crack is manufactured by a Teflon insert with a thickness of about $10 \mu\text{m}$. The fracture energy

is directly obtained by the experimentally recorded failure load, cf. the discussion in section 3.2. The remaining details of the cohesive law are determined by matching the experimental load versus relative displacement of measuring points at the crack tip to FE-simulations. The local displacement field near the crack tip is measured using DIC technique. Due to the limited resolution of the DIC measurements, measuring points for the crack tip opening is placed about 0.5 mm above and below the crack tip.

5 Longitudinal compressive failure

Fibre failure is a very critical event in CFRP components since almost all the load is carried by the fibres. It is widely known that the longitudinal compressive strength is substantially lower than the tensile strength, e.g. [140]. Thus, experimental characterisation that enables modelling of the behaviour under longitudinal compression is critical for safe design of structural components.

5.1 Kink-band formation

The longitudinal compressive strength is far more difficult to predict than the tensile strength. This is due to the complicated failure mode displayed by CFRP:s under longitudinal compression. Kink-band formation sometimes denoted micro-buckling¹ are widely recognized as the primary failure mode in longitudinal compression [142, 143, 144].

Micro-buckling may be triggered at fibres of high curvature from fibre waviness, at a void or similar defect or at free edges where fibres lack lateral support [145]. With classical theories of plastic micro-buckling, the compressive strength is governed by the initial fibre misalignment and the shear behaviour of the matrix [146, 147, 142]. Plastic micro-buckling is the failure mode where compressive loading induces bending of the misaligned fibres. The matrix is forced to deform in a shearing mode and as the loading increase, the matrix yields. Eventually, the axial compression and bending stresses cause fibre failure. This process creates a localized band of broken fibres, denoted a kink-band, that propagates into the undamaged material under increasing load.

Fig. 5.1a display a sketch of a kink-band with commonly used geometric parameters. These are the kink-band width, w_k , the fibre orientation, α and the kink-band orientation β . For CFRP, typical values are $\alpha \approx 30^\circ - 45^\circ$, $\beta \approx 20^\circ$ and $w_k \approx 70 - 200 \mu\text{m}$ [141]. In Fig. 5.1b, a kink-band from paper D is shown.

The processes that govern compressive failure are difficult to observe in-situ since compressive failure often occurs in a sudden and unstable manner. However, in [149], an in-plane kink-band formation is observed in a scanning electron microscope while the specimen is kept under load. It is demonstrated that microcracking in-between fibres and fibre/matrix debonding is responsible for the loss of support of the fibres. It is further shown that fibre failure occurred through shear failure at the most compressed side of

¹There is no consensus on what differentiates micro-buckling and kink-band formation. Some authors consider kink-band formation as a result of micro-buckling while they are considered as two different failure modes [141].

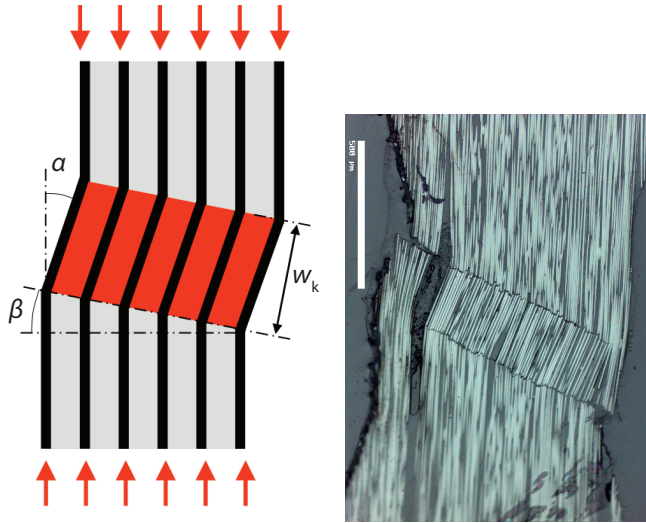


Figure 5.1: a) Kink-band geometry. Picture from [148, 141]. b) Kink-band observed in paper D. Scale bar indicates $500 \mu\text{m}$.

the bended fibres. However, it is shown that the initial failure mode was not kink-band formation. Instead, brittle shear failure occurred approximately 45° to the fibres. After some propagation distance, the failure mode was transformed to kink-band propagation. Based on experimental observations and micro-mechanical modelling, the stress states inherent to each failure mode is presented in [150, 148]. It is demonstrated that kink-band formation occurs when a sufficient amount of shear stress along the fibres are present. For nearly pure longitudinal stress states, brittle shear failure of the fibres occurs. When the shear stress along the fibres is dominating, intralaminar failure occurs. Thus, kink-band formation requires some amount of shear stresses along the fibres which may be introduced by e.g. fibre waviness or by the applied loading by specimen misalignment. Numerous analytical models for the prediction of the compressive strength have been proposed in the literature, cf. e.g. [150] for an overview.

5.2 Measurement of the fracture energy

Compressive failure is often induced at notches or holes. Thus, predicting failure by elastic analyses and strengths obtained from unnotched coupon tests may be overly conservative, cf. the example in section 1.1. Thus models for prediction of the progressive damage growth, e.g. CZM:s or continuum damage models, have been proposed [151, 152]. These models require both the strength and the fracture energy as input parameters. Moreover, in [153], Soutis et al. demonstrate that the open hole compression strength in laminates of varying stacking sequence is governed by micro-buckling in the plies with the fibre

orientation aligned with the loading direction. Therefore, it is desirable to determine the fracture energy associated with longitudinal compression.

Since the early 1990's, several methods have been presented for the experimental determination of the fracture energy associated with longitudinal compression, cf. [144] for a discussion. Pinho et al. [144] use a Compact Compression specimen with a cross-ply laminate. The fracture energy is calculated at the maximum load. By conducting a linear elastic finite element simulation and J -integral calculations, the relation between the applied load and the energy release rate is determined. Later in [154], four-point-bending tests are conducted using notched unidirectional specimens. Similar to [144], a relation is calculated between the energy release rate and the applied load by using linear finite element analysis. It is observed that failure occurred by brittle shear failure. These methods all rely on that the FPZ is of negligible size. However, this assumption is avoided in [155]. In [155], the authors conduct experiments with the compact compression cross ply specimen suggested by Pinho [144]. The energy release rate is measured by evaluating the J -integral from the actual strain field using Digital Image Correlation (DIC). The integration path encircles the complete notch. Recently, a framework for measurement of the complete resistance curve associated with kink-band propagation is proposed in [156].

With the exception of [154], all references above consider compressive failure in cross-ply laminates. Thus, partitioning of the fracture energy is needed and interaction effects between off-axis plies are neglected [154]. This suggests that measurement of the fracture energy should be conducted with UD-laminates. However, a possible draw-back with using UD-laminates is that kinking tends to mainly occur in the out-of-plane direction. For multidirectional laminates, as always used in real structural components, kinking usually develops in-plane. However, in [145] it is pointed out that cross-ply also promote out-of-plane kinking. Moreover, it is shown that, for varying lay-ups of $(\pm\theta/0_2)_{2S}$, in-plane kinking is observed for $\theta = 30^\circ$, $\theta = 45^\circ$ and $\theta = 60^\circ$.

5.3 Objective and method in paper D

In paper D, the objective is to experimentally extract the cohesive law associated with kink-band formation in a UD-laminate. With the present specimen, the out-of-plane thickness is continuously reduced towards the zone that fails in compression. This geometry is used in order to achieve longitudinal compressive failure in a UD laminate. A microscopic study shows a kink-band with a large out-of-plane component in the UD-region, cf. Fig. 5.1b. The cohesive law represents the material volume with a height of $200\ \mu\text{m}$ similar to the kink-band height displayed in Fig. 5.1b. The proposed data reduction scheme is based on the concept of configurational forces [157] and DIC measurement of the strain field. For this kind of geometry, this concept is strongly related to the J -integral concept, cf. section 2.2. Thus, no assumption of a small FPZ is made. The extracted cohesive laws suggest strengths similar to usually reported for prepregs while the fracture energy is well below those reported in the references in section 5.2. The relatively high strengths measured are considered reasonable for this test geometry. The material volume subjected to substantial compressive stress in the presented experiments is considerably smaller than in conventional unnotched bulk tests. That is, the risk that defects are present within the

tested volume is lower in the present tests than in conventional unnotched tests. Since measurement of the compressive strength is very sensitive to initial material defects, this implies that higher strength measures are promoted with the presented geometry. Such size effect is reported for specimens failing by kink-band formation in [158].

6 Summary of appended papers

Paper A

A method to extract the cohesive laws associated with mode I and II delamination in a CFRP laminate is presented. The evaluation method is based on data from DCB and ENF tests and involves measurements of the displacement field near the crack tip using digital image correlation. Finite element simulations and an optimization procedure are utilized to extract the cohesive laws. For loading in mode I, the fracture energy and cohesive strength are in the order of 300 J/m^2 and 75 MPa , respectively. The corresponding values for mode II loading are 1200 J/m^2 and 80 MPa . In mode I, the cohesive law displays a softening response shortly after the strength is reached while a substantial part of constant shear stress is obtained prior to softening for mode II.

Paper B

An experimental method to extract cohesive laws associated with mixed mode delamination is developed. The method is based on MMB tests and measurements of the displacement field near the crack tip. An initiation driven mixed mode cohesive law is proposed, for which the behaviour in the cohesive zone is given by the conditions at the crack tip. This facilitates a straightforward evaluation of the cohesive parameters from experimentally obtained fracture energies and critical separations near the crack tip. Verifying finite element simulations show that the experimentally determined cohesive law reproduces the load versus the local displacement near the crack tip with good accuracy.

Paper C

The influence of initial cohesive stiffnesses and the formulation of the nonlinear behaviour of mixed mode cohesive laws are under discussion. More specifically, properties of cohesive laws are specified that enable degeneration to LEFM results under mixed mode small scale yielding conditions. By analytical derivations, two conditions are concluded sufficient to achieve this. The first condition is a constraint that relates the initial stiffnesses to the elastic stiffnesses of the orthotropic material. The second condition states that the mode mix in terms of the mode I and II energy cannot vary when the associated separations are constantly related. It is shown that the second condition cannot be fulfilled with a potential-based cohesive law that possesses a mode dependent cohesive fracture energy. These conclusions are validated with FE-analyses of an orthotropic

planar body subjected to loading assuming SSY conditions. It is demonstrated that, provided that both conditions are met, the mode I and II energy release rates agree with the counterparts given by the prescribed edge displacements. Furthermore, two cohesive laws referred to as stress-based and initiation-driven laws can be designed to fulfil the conditions and allow for a mode dependent fracture energy. Simulations are also conducted on the MMB-geometry to investigate the effect of a finite geometry. It is shown that the conditions minimize the discrepancy to LEFM predictions.

Paper D

A method to extract the cohesive law associated with longitudinal compressive failure is presented. Equilibrium of configurational forces is used to design and evaluate the experiments. Microscopic studies show that a kink-band with the height of about 200 μm is formed in the UD-laminate. The corresponding cohesive laws shows a peak stress of about 1.5 GPa, a compression at failure of about 50 μm and a fracture energy of about 25 kJ/m^2 .

7 Future work

During this work, several possibilities for future developments have been identified.

Paper A and B focus on the extraction of cohesive laws associated with delamination. The determination of cohesive parameters relies on measurement of the displacement field of the crack tip region. For this purpose, DIC-measurements are utilized and the displacements of two points located about 1 mm apart are used in the evaluation. It is reasonable to assume that the inelastic behaviour present at the proximity of the crack tip is embedded in a region substantially smaller than that. Thus, measurement on a lower scale is desirable. An ambitious goal would be to experimentally measure the height of the FPZ and position the measuring points based on that knowledge.

In paper C, the design rules for the formulation of cohesive laws are presented. With these rules satisfied, CZM:s degenerate to the LEFM predictions under SSY conditions. This allows for a number of interesting continuations. For example, an extension of the design rules to handle bi-material interface and mode III loading to allow for 3D simulations of delamination between plies of different orientations.

In paper D, a method is presented for the measurement of cohesive laws associated with kink-band formation in a UD-laminate. Earlier attempts to experimentally determine cohesive laws have not been identified. The presented work shows promising potential but involves a rather elaborate data reduction scheme. A simplification of the test set-up that allows for a larger number of tests is desirable. Such a method is under development.

References

- [1] R. Koide, G. von Zeska de França, and M. Luersen. An ant colony algorithm applied to lay-up optimization of laminated composite plates. *Latin American Journal of Solids and Structures* **10(3)** (2013), (On-line version ISSN 1679-7825).
- [2] *Boeing 787 from the ground up. QTR 04 06.*
- [3] url = "http://modernairliners.com/Boeing787files/Specifications.html".
- [4] H. Fenbert. "Composites in commercial aircraft a production cost perspective". *ICCM/9: Composites properties and applications*. 1993.
- [5] *Composite Materials Handbook, MIL-HDBK-17-3F, U.S. Department of Defence, 2002.*
- [6] A. Mouritz. *Introduction to Aerospace Materials*. Woodhead Publishing Ltd, Cambridge, 2012, (ISBN 9871855739468), pp.621., 2012.
- [7] T. Nyman. "Fatigue and residual strength of composite aircraft structures". PhD thesis. KTH, Aeronautical Engineering, 1999.
- [8] Private communication with Tonny Nyman at SAAB Aerostructures Linköping.
- [9] P. Treasurer. "Characterization and analysis of damage progression in non-traditional composite laminates with circular holes". MA thesis. Georgia Institute of Technology, 2006.
- [10] M. Wisnom, B. Khan, and S. Hallett. Size effects in unnotched tensile strength of unidirectional and quasi-isotropic carbon/epoxy composites. *Composite Structures* **84** (2008), 21–28.
- [11] M. Wisnom, S. Hallett, and C. Soutis. Scaling effects in notched composites. *Journal of Composite Materials* **44** (2010), 195–210.
- [12] J. Lee and C. Soutis. Measuring the notched compressive strength of composite laminates: Specimen size effects. *Composite Science and Technology* **68** (2008), 2359–2366.
- [13] F. Edgren. "Physically based engineering models for NCF composites". PhD thesis. Royal Institute of Technology, Sweden, 2006.
- [14] F. Edgren, L. Asp, and R. Joffe. Failure of NCF composites subjected to combined compression and shear loading. *Composite Science and Technology* **66(15)** (2006), 2865–77.
- [15] M. Laffan et al. Translaminar fracture toughness testing of composites: A review. *Polymer Testing* **31** (2012), 481–489.
- [16] C. Inglis. Stresses in a plate due to the presence of cracks and sharp corners. *Trans. Inst. Nav. Archit. London* **55** (1913), 219–230.
- [17] A. Griffith. The phenomena of rupture and flow in solids. *Phil. Trans. R. Soc. A* **221** (1921), 163–98.
- [18] G. Irwin. Onset of fast crack propagation in high strength steel and aluminum alloys. *Sagamore Research Conference proceedings* **2** (1956), 289–305.
- [19] H. Tada, P. Paris, and G. Irwin. *Stress analysis of cracks handbook*. Del Reasearch, St. Louis, MO, 1985.
- [20] Z. Sou et al. Orthotropy rescaling and implications for fracture in composites. *International Journal of Solids and Structures* **28(2)** (1991), 235–248.

- [21] G. Bao et al. The role of material orthotropy in fracture specimens for composites. *International Journal of Solids and Structures* **29** (1991), 1105–1116.
- [22] url = "http://en.wikipedia.org/wiki/Stressintensityfactor".
- [23] G. Sih, P. Paris, and G. Irwin. On cracks in rectilinearly anisotropic bodies. *International Journal of Fracture Mechanics* **1** (1965), 189–203.
- [24] *Linear elastic fracture mechanics 2014 03 08*. url = "http://imechanica.org/files/Linear elastic fracture mechanics 2014 03 08.pdf".
- [25] S. Lekhnitskii. *Theory of elasticity of an anisotropic body*. Mir publisher, Moscow, 1981.
- [26] K. Alfredsson and U. Stigh. Stability of beam-like fracture mechanics specimens. *Engineering Fracture Mechanics* **89** (2012), 98–113.
- [27] M. Juntti, L. Asp, and R. Olsson. Assessment of Evaluation Methods for the Mixed-Mode Bending Test. *Journal of Composites Technology and Research* **21** (1999), 37–48.
- [28] J. Rice. A path independent integral and the approximative analysis of strain concentration by notches and holes. *Journal of Applied Mechanics* **88** (1968), 379–386.
- [29] A. Needleman. "Some issues in cohesive surface modelling". *23rd International Congress of Theoretical and Applied Mechanics*. 2014.
- [30] J. Rice. "The mechanics of quasi-static crack growth". *Proceedings of the eighth U.S. National congress of applied mechanics*. 1979.
- [31] F. Nilsson. *Fracture Mechanics - from Theory to applications*. Fingraf, Södertälje, Sweden, 2001.
- [32] B. Budiansky. A reassessment of deformation theories of plasticity. *Journal of Applied Mechanics* **26** (1959), 259–264.
- [33] V. Tvergaard and J. Hutchinson. The relation between crack growth resistance and fracture process parameters in elastic-plastic solids. *Journal of the Mechanics and Physics of Solids* **40** (1992), 1377–97.
- [34] T. L. Anderson. *Fracture Mechanics: Fundamentals and Applications, Third Edition*. Boca Raton, FL: Taylor & Francis/CRC Press, 2005.
- [35] M. R. Wisnom. Modelling discrete failure in composites with interface elements. *Composites Part A* **41** (2010), 795–805.
- [36] G. Barenblatt. The mathematical theory of equilibrium cracks in brittle fracture. *Advances in Applied Mechanics* **7** (1962), 55–129.
- [37] D. Dugdale. Yielding of steel sheets containing slits. *Journal of the Mechanics and Physics of Solids* **8** (1960), 100–104.
- [38] A. Hillerborg, M. Modeér, and P. Peterson. Analysis of crack formation and crack growth in concrete by means of fracture mechanics and finite elements. *Cement and Concrete Research* **6** (1976), 773–782.
- [39] A. Needleman. A continuum model for void nucleation by inclusion debonding. *Journal of Applied Mechanics* **54** (1987), 525–532.
- [40] Q. Yang and M. Thouless. Mixed mode fracture of plastically-deforming adhesive joints. *International Journal of Fracture* **110** (2001), 175–187.
- [41] X. Xu and A. Needleman. Void nucleation by inclusion debonding in crystal matrix. *Model Simul Mater Sci* **1** (1993), 111–132.

- [42] O. Allix and P. Ladeveze. Interlaminar interface modeling for the prediction of delamination. *Composite Structures* **22**(4) (1992), 235–242.
- [43] J. Schellekens and R. De Borst. A non-linear finite element approach for the analysis of mode I free edge delamination in composites. *International Journal of Solids and Structures* **30**(9) (1993), 1239–1253.
- [44] W. Cui and M. R. Wisnom. A combined stress-based and fracture-mechanics-based model for predicting delamination in composites. *Composites* **24** (1993), 467–74.
- [45] B. Sørensen and P. Kirkegaard. Determination of mixed mode cohesive laws. *Engineering Fracture Mechanics* **73** (2006), 2642–2661.
- [46] V. Tvergaard. Effect of fibre debonding in a whisker-reinforced metal. *Material Science and Engineering A* **125** (1990), 203–13.
- [47] G. Camacho and M. Ortiz. Computational modelling of impact damage in brittle materials. *International Journal of Solids and Structures* **33** (1996), 2899–938.
- [48] M. van der Bosch, P. Schreurs, and M. Geers. An improved description of the exponential Xu and Needleman cohesive zone law for mixed-mode decohesion. *Engineering Fracture Mechanics* **73** (2006), 1220–1234.
- [49] S. Goutianos and B. Sørensen. Path dependence of truss-like mixed mode cohesive laws. *Engineering Fracture Mechanics* **91** (2012), 117–132.
- [50] R. Sills and M. Thouless. The effect of cohesive-law parameters on mixed-mode fracture. *Engineering Fracture Mechanics* **109** (2013), 353–368.
- [51] V. Tvergaard and J. Hutchinson. The Influence of plasticity on mixed mode interface toughness. *Journal of the Mechanics and Physics of Solids* **41**(6) (1993), 1119–35.
- [52] X. Xu and A. Needleman. Numerical simulations of fast crack growth in brittle solids. *Journal of the Mechanics and Physics of Solids* **42**(9) (1994), 1397–434.
- [53] B. Sørensen et al. Micromechanical model of cross-over fibre bridging prediction of mixed mode bridging laws. *Mechanics of materials* **40** (2008), 220–34.
- [54] K. Park, G. Paulino, and J. Roesler. A unified potential-based cohesive model of mixed mode fracture. *Journal of the Mechanics and Physics of Solids* **57** (2009), 891–908.
- [55] J. McGarry et al. Potential-based and non-potential-based cohesive zone formulations under mixed-mode separation and over-closure. Part I: Theoretical analysis. *Journal of the Mechanics and Physics of Solids* **63** (2014), 336–362.
- [56] E. Mairtin et al. Potential-based and non Potential-based cohesive zone formulations under mixed-mode separation and over-closure - Part II: Finite element applications. *Journal of the Mechanics and Physics of Solids* **63** (2014), 363–385.
- [57] P. Camanho, C. Davila, and M. de Moura. Numerical simulation of mixed-mode progressive delamination in composite materials. *Journal of Compiste Materials* **37**(16) (2003), 1415–38.
- [58] A. Turon et al. A damage model for the simulation of delamination in advanced composites under variable-mode loading. *Mechanics of materials* **38** (2006), 1079–1089.
- [59] A. Turon et al. Accurate simulation of delamination growth under mixed-mode loading using cohesive elements: Definition of interlaminar strength and elastic stiffness. *Composite Structures* **92** (2010), 1857–1864.

- [60] J. Högberg. Mixed mode cohesive law. *International Journal of Fracture* **141** (2006), 549–559.
- [61] N. Jansson and R. Larsson. A damage model for simulation of mixed-mode delamination growth. *Composite Structures* **53** (2001), 409–417.
- [62] J. Högberg, B. Sörensen, and U. Stigh. Constitutive behaviour of mixed mode loaded adhesive layer. *International Journal of Solids and Structures* **44** (2007), 8335–54.
- [63] L. Ye. Role of Matrix Resin in Delamination onset and growth in composite laminates. *Composite Science and Technology* **33** (1988), 257–277.
- [64] N. Chandra et al. Some issues in the application of cohesive zone models for metal-ceramic interfaces. *International Journal of Solids and Structures* **39** (2002), 2827–2855.
- [65] J. Hutchinson and A. Evans. Mechanics of materials: top-down approach to fracture. *Acta Metallurgica* **48** (2000), 125–35.
- [66] P. Harper, L. Sun, and S. Hallet. A study on the influence of cohesive zone interface element strength parameters on mixed mode behaviour. *Composites Part A* **43** (2012), 722–734.
- [67] P. Gustafson and A. Waas. The influence of adhesive constitutive parameters in cohesive zone finite element models of adhesively bonded joints. *International Journal of Solids and Structures* **46** (2009), 2201–2215.
- [68] G. Alfano. On the influence of shape of the interface law on the application of cohesive-zone models. *Composite Science and Technology* **66** (2006), 723–730.
- [69] M. R. Wisnom. Modelling of stable and unstable fracture of short beam shear specimens. *Composites* **25** (1994), 394–400.
- [70] Z. Petrossian and M. R. Wisnom. Prediction of delamination initiation and growth from discontinuous plies using interface elements. *Composites Part A: Applied Science and Manufacturing* **29.56** (1998), 503–515.
- [71] A. Uguen et al. “Comparison of cohesive zone models used to predict delamination initiated from free-edges: validation against experimental results”. *ECCM-16TH European Conference on Composite Materials*. 2014.
- [72] M. Elices et al. The cohesive zone model: advantages, limitations and challenges. *Engineering Fracture Mechanics* **69** (2002), 137–163.
- [73] J. Rots. *Strain-softening analysis of concrete fracture specimens*. Ed. by e. Wittmann FH. In: Wittmann FH, editor. *Fracture toughness and fracture energy of concrete*. Amsterdam, The Netherlands: Elsevier Science Publishers, 1986, p. 137–48.
- [74] C. Shet and N. Chandra. Effect of the Shape of $t - \delta$ Cohesive Zone Curves on the Fracture Response. *Mechanics of Advanced Materials and Structures* **11** (2004), 249–275.
- [75] M. Jalalvand, G. Czél, and M. Wisnom. “Numerical modelling of the damage modes in UD thin carbon/glass hybrid laminates - sensitivity analysis”. *Camanho, P.P. and Soleman, A., editors. Compos. 2013 Conf., Ponta Del Gada. p. 1-15*. 2013.
- [76] U. Stigh and T. Andersson. “An experimental method to determine the complete stress-elongation relation for a structural adhesive layer loaded in peel”. *Proceedings of the 2nd ESIS TC4 Conference on Polymers and Composites*. Amsterdam:

- Elsevier*; p. 297-306 [ESIS Publication 27], Eds. J.G. Williams and A. Pavan. 2000.
- [77] B. Sørensen. Cohesive law and notch sensitivity of adhesive joints. *Acta Mater* **50** (2002), 1053–61.
 - [78] T. Andersson and U. Stigh. The stress-elongation relation for an adhesive layer loaded in peel using equilibrium of energetic forces. *International Journal of Solids and Structures* **41** (2004), 413–34.
 - [79] S. Li et al. Mixed-mode cohesive-zone models for fracture of an adhesively bonded polymer-matrix composite. *Engineering Fracture Mechanics* **73(1)** (2006), 64–78.
 - [80] K. Leffler, K. Alfredsson, and U. Stigh. Shear behaviour of adhesive layers. *International Journal of Solids and Structures* **44** (2007), 530–45.
 - [81] Y. Zhu, K. Liechti, and K. Ravi-Chandar. Direct extraction of rate-dependent traction-separation laws for polyurea/steel interfaces. *International Journal of Solids and Structures* **46** (2009), 31–51.
 - [82] B. Sørensen and T. Jacobsen. Large-scale bridging in composites: R-curves and bridging laws. *Composites Part A: Applied Science and Manufacturing* **29.11** (1998), 1443–1451.
 - [83] L. Sorensen et al. Bridging tractions in mode I delamination; measurement and simulations. *Composite Science and Technology* **68** (2008), 2350–8.
 - [84] B. Sørensen and T. K. Jacobsen. Characterizing delamination of fibre composites by mixed mode cohesive laws. *Composite Science and Technology* **69** (2009), 445–56.
 - [85] C. Sun and Z. Jin. Modeling of composite fracture using cohesive zone and bridging models. *Composite Science and Technology* **66** (2006), 1297–302.
 - [86] M. Jalalvand, G. Czel, and M. R. Wisnom. “Extracting cohesive laws from displacement field measurement”. *29th Annual Technical Conference of the American Society for Composites 2014*. 2014.
 - [87] G. Ljustina, M. Fagerström, and R. Larsson. Rate Sensitive Continuum Damage Models and Mesh Dependence in Finite Element Analyses. *The Scientific World Journal* **2014:260571** (2014), DOI: 10.1155/2014/260571.
 - [88] P. Harper and S. Hallet. Cohesive zone length in numerical simulations of composite delamination. *Engineering Fracture Mechanics* **75** (2008), 4774–92.
 - [89] A. Turon et al. An engineering solution for mesh size effects in the simulation of delamination using cohesive zone models. *Engineering Fracture Mechanics* **74** (2007), 1665–1682.
 - [90] V. Tomar, J. Zhai, and M. Zhou. Bounds for element size in a variable stiffness cohesive finite element model. *International Journal of Numerical Methods* **61(11)** (2004), 1894–1920.
 - [91] C. Fan, P. Jar, and J. Cheng. Cohesive zone with continuum damage properties for simulation of delamination development in fibre composites and failure of adhesive joints. *Engineering Fracture Mechanics* **75(13)** (2008), 3866–3880.
 - [92] J. Schellekens and R. de Borst. On the numerical integration of interface elements. *International Journal for Numerical Methods in Engineering* **36** (1992), 43–66.
 - [93] C. Sarrado et al. Assessment of energy dissipation during mixed-mode delamination growth using cohesive zone models. *Composites Part A* **43** (2012), 2128–2136.

- [94] E. S. Greenhalgh and M. Hiley. The assessment of novel materials and processes for the impact tolerant design of stiffened composite aerospace structures. *Composites Part A: Applied Science and Manufacturing* **34** (2003), 151–161.
- [95] L. Asp, S. Nilsson, and S. Singh. An experimental investigation of the influence of delamination growth on the residual strength of impacted laminates. *Composites Part A* **32** (2001), 1229–35.
- [96] T. Tay. Characterization and analysis of delamination fracture in composites: An overview of developments from 1990 to 2001. *Appl Mech Rev* **56** (2003), no 1.
- [97] I. Daniel and O. Ishai. *Engineering mechanics of composite materials*. Ed. by I. Daniel. Oxford university press, 2006.
- [98] A. Garg. Delamination - a damage mode in composite structures. *Engineering Fracture Mechanics* **29** (1988), 557–584.
- [99] S. Sridharan. *Delamination behaviour of composites*. Ed. by S. Sridharan. In Woodhead Publishing Series in Composites Science and Engineering, 2008.
- [100] A. Weiss et al. Influence of ply-drop location on the fatigue behaviour of tapered composites laminates. *Procedia Engineering* **2.1** (2010), 1105 –1114.
- [101] C. Soutis and P. Curtis. Prediction of post-impact compressive strength of CFRP laminated composites. *Composite Science and Technology* **56** (1996), 677–684.
- [102] Q. Yang and B. Cox. Cohesive models for damage evolution in laminated composites. *International Journal of Fracture* **133** (2005), 107–137.
- [103] M. Hibbs and W. Bradley. *Correlations Between Micromechanical Failure Processes and the Delamination Toughness of Graphite/Epoxy Systems*. Fractography of Modern Engineering Materials: Composites and Metals, ASTM STP 948, American Society for Testing and Materials, 68-97, 1987.
- [104] E. Greenhalgh, C. Rogers, and P. Robinson. Fractographic observations on delamination growth and subsequent migration through the laminate. *Composite Science and Technology* **69** (2009), 2345–2351.
- [105] T. O'Brien. "Interlaminar shear fracture toughness, G_{IIC} : shear measurement or sheer myth?" *7th ASTM Symposium on Composite Materials: Fatigue and Fracture*. 1998.
- [106] A. Sjögren et al. Interlaminar Crack Propagation in CFRP: Effects of Temperature and Loading Conditions on Fracture Morphology and Toughness. *ASTM STP 1416 & ASTM D-30* (2002).
- [107] L. Asp, A. Sjögren, and E. Greenhalgh. Delamination Growth and Thresholds in a Carbon/Epoxy Composite Under Fatigue Loading. *Journal of Composites Technology and Research* **23** (2001), 55–68.
- [108] E. Greenhalgh. "Characterisation of mixed-mode delamination growth in carbon-fibre composites." PhD thesis. Imperial Collage, UK, 1998.
- [109] W. Bradley. *Relationship of matrix toughness to interlaminar fracture toughness*. Ed. by K. Friedrich. Applications of fracture mechanics to composite materials, Amstredam, Elsevier, pp. 159-187, 1989.
- [110] R. Olsson. *Factors influencing the interlaminar fracture toughness and its evaluation in composites*. Tech. rep. FFA TN 1991-34, 1991.
- [111] D. Parker. "Factors affecting the mode I interlaminar fracture resistance of toughened matrix composites". PhD thesis. University of Michigan, 1989.

- [112] J. Crews, K. Shivakumar, and I. Raju. *A fibre-resin micromechanics analysis of the delamination front in a DCB specimen*. Tech. rep. 1988.
- [113] M. Benzeggah and M. Kenane. Measurement of mixed-mode delamination fracture toughness of unidirectional glass/epoxy composites with mixed-mode bending apparatus. *Composite Science and Technology* **56** (1996), 439–49.
- [114] J. Reeder. “3D mixed-mode Delamination fracture criteria - an experimentalists perspective”. *Proceeding of American society for composites 21st annual technical conference*, p. 1-18. Dearborn (MI); United States. 2006.
- [115] P. Davies, B. Blackman, and A. Brunner. Standard test methods for delamination resistance of composite materials: current status. *Applied composite materials* **5(6)** (1998), 345–64.
- [116] A. Brunner, B. Blackman, and P. Davies. A status report on delamination resistance testing of polymer-matrix composites. *Engineering Fracture Mechanics* **75** (2008), 2779–2794.
- [117] *ASTM. D5528 Standard test method for mode I interlaminar fracture toughness of unidirectional fiber-reinforced polymer matrix composites*. 2007.
- [118] *Testing methods for interlaminar fracture toughness of carbon fibre reinforced plastics, K7086, Japanese Standard Association, JSA;1993*.
- [119] *ASTM Committee D-30. Standard test method for determination of the mode II interlaminar fracture toughness of unidirectional fiber reinforced polymer matrix composites using the End-Notch Flexure (ENF) test. ASTM draft standard; 2010*.
- [120] *ASTM D 6671-01. Standard test method for mixed mode I-mode II interlaminar fracture toughness of unidirectional fiber reinforced polymer matrix composites. ASTM Standards 2001*.
- [121] J. Reeder and J. Crews Jr. Mixed-Mode Bending Method for Delamination Testing. *AIAA Journal* **28** (1990), 1270–1276.
- [122] J. Reeder and J. Crews. *Notesting analysis and redesign of the mixed-mode bending delamination test*. Tech. rep. NASA TM 102777, 1991.
- [123] J. Andersons and M. Konig. Dependence of fracture toughness of composite laminates on interface ply orientations and delamination growth direction. *Composite Science and Technology* **64** (2004), 2139–52.
- [124] B. Kim and A. Mayer. Influence of fibre direction and mixed-mode ratio on delamination fracture toughness of carbon/epoxy laminates. *Composite Science and Technology* **63** (2003), 695–713.
- [125] N. De Carvalho et al. Modeling delamination migration in cross-ply tape laminates. *Composites Part A* **71** (2015), 192–203.
- [126] T. Sebaey et al. Characterization of crack propagation in mode I delamination of multidirectional CFRP laminates. *Composite Science and Technology* **72** (2012), 1251–1256.
- [127] N. Choi, A. Kinloch, and J. Williams. Delamination Fracture of multidirectional Carbon-Fiber/Epoxy Composites under Mode I, Mode II and Mixed-Mode I/II Loading. *Journal of Composite Materials* **33(1)** (1999), 73–100.
- [128] P. Naghipour et al. Fracture simulation of CRFP laminates in mixed mode bending. *Engineering Fracture Mechanics* **72** (2009), 1718–1724.

- [129] P. Davies et al. Measurement of G_{IC} and G_{IIC} in carbon/epoxy composites. *Composite Science and Technology* **39** (1990), 193–205.
- [130] A. Brunner. Experimental aspects of Mode I and Mode II fracture toughness testing of fibre-reinforced polymer-matrix composites. *Computer methods in applied mechanics and engineering* **185** (2000), 161–172.
- [131] K. Cowley and P. Beaumont. The interlaminar and intralaminar fracture toughness of carbon-fibre/polymer composites: the effect of temperature. *Composite Science and Technology* **57** (1997), 1433–44.
- [132] Z. Sou, G. Bao, and B. Fan. Delamination R-curve phenomena due to damage. *Journal of the mechanics and physics of solids* **40(1)** (1992), 1–16.
- [133] B. Sørensen and T. K. Jacobsen. Determination of cohesive laws by the J -integral approach. *Engineering Fracture Mechanics* **70** (2003), 1841–58.
- [134] url="http://www.compositesworld.com/articles/methods-for-interlaminar-tensile-testing-of-composites-a-comparative-evaluation".
- [135] *ASTM Standard D 6415/D 6415M. Standard test method for measuring the curved beam strength of a fiber-reinforced polymer-matrix composite; 2006.*
- [136] *ASTM Standard D 2344/D 2344M. Standard test method for short-beam strength of polymer matrix composite materials and their laminates; 2006.*
- [137] A. Makeev et al. Methods for assessment of interlaminar tensile strength of composite materials. *Journal of composite materials* (2014), 0021998314525979.
- [138] Y. He and A. Makeev. Nonlinear shear behavior and interlaminar shear strength of unidirectional polymer matrix composites: A numerical study. *International Journal of Solids and Structures* **51** (2014), 1263–1273.
- [139] R. Olsson et al. Investigations of Delamination Criticality and Transferability of Growth Criteria. *Composite Structures* **36** (1996), 221–247.
- [140] C. Soutis. Compressive strength of unidirectional composites; measurement and predictions. *ASTM STP* **1242** (1997), 168–176.
- [141] S. Pimenta. “Micromechanics of kink-band formation”. PhD thesis. Imperial Collage, UK, 2008.
- [142] B. Budiansky and N. Fleck. Compressive failure of fibre composites. *J. Mechanics and Physics of Solids* **41.1** (1993), 183–211.
- [143] N. Fleck, S. Sivashanker, and S. M.P.F. Compressive failure of composites due to microbuckle growth. *Eur. J. Mech. Solids* **16** (1997), 65–82 (Special issue).
- [144] S. Pinho, P. Robinson, and L. Iannucci. Fracture toughness of tensile and compressive fibre failure modes in laminated composites. *Composites Science and Technology* **66** (2006), 2069–2079.
- [145] P. Berbinau et al. Effect of off-axis ply orientation on 0° -fibre microbuckling. *Composites Part A* **30** (1999), 1197–1207.
- [146] A. Argon. *Fracture of composites, Treatise on Materials Science and Technology*, Academy Press, New York, 1972.
- [147] B. Budiansky. Micromechanics. *Computer and Structures* **16** (1983), 3–12.
- [148] S. Pinho et al. On longitudinal compressive failure of carbon-fibre-reinforced polymer: from unidirectional to woven, and from virgin to recycled. *Phil. Trans. R. Soc. A* **370.165** (2012), 1871–1895.

- [149] R. Gutkin et al. On the transition from shear-driven fibre compressive failure to fibre kinking in notched CFRP laminates under longitudinal compression. *Composites Science and Technology* **70** (2010), 1223–1231.
- [150] R. Gutkin et al. Micro-mechanical modelling of shear-driven fibre compressive failure and of fibre kinking for failure envelope generation in CFRP laminates. *Composites Science and Technology* **70** (2010), 1214–1222.
- [151] P. Camanho, P. Maimí, and C. Davila. Prediction of size effects in notched laminates using continuum damage mechanics. *Composite Science and Technology* **67** (2007), 2715–2727.
- [152] C. Rose, C. Davila, and F. Leone. *Analysis Methods for Progressive Damage of Composite Structures*. Tech. rep. NASA/TM 2013-218024, 2013.
- [153] C. Soutis, N. Fleck, and P. Smith. Failure prediction technique for compression loaded carbon fiber-epoxy laminate with open holes. *Journal of Composite Materials* **25** (1991), 1476–98.
- [154] M. Laffan et al. Measurement of the fracture toughness associated with the longitudinal fibre mode of laminated composites. *Composites Part A* **43** (2012), 1930–1938.
- [155] G. Catalanotti et al. Measurement of resistance curves in the longitudinal failure of composites using digital image correlation. *Composites Science and Technology* **70.13** (2010), 1986–93.
- [156] G. Catalanotti, J. Xavier, and P. Camanho. Measurement of the compressive crack resistance curve of composites using the size effect law. *Composites Part A* **56** (2014), 300–307.
- [157] J. Eshelby. The force on an elastic singularity. *Phil. Trans. R. Soc. London* **244** (1951), 87–112.
- [158] Z. Bažant et al. Size effect on compression strength of fiber composites failing by kink band propagation. *International Journal of Fracture* **95** (1999), 103–141.